Rare Events Prediction:

Rogue Waves and Drags

by

Ming Tong

A thesis

presented to the University Of Waterloo

in fulfilment of the

thesis requirement for the degree of

Master of Science

in

Physics

Waterloo, Ontario, Canada, 2018

# Author's Declaration

I hereby declare that I am the sole author of this thesis. This is a true copy of the thesis, including any required final revisions, as accepted by my examiners.

I understand that my thesis may be made electronically available to the public.

# Abstract

Rogue waves are rare events with unusually large wave amplitudes. In this thesis the multicanonical procedure is applied to the one-dimensional nonlinear Schrödinger equation in conjunction with a high order finite difference solution procedure to determine the probability distribution function of rogue wave power and heights. The analysis demonstrates a logarithmic dependence of the slope of the probability distribution function on the nonlinearity coefficient at large heights. The results of the multicanonical procedure helps explain the mechanism of rogue waves and confirms that the nonlinearity generates rogue waves.

Small deformation of an obstacle in fluid flows can in extreme cases result in anomalous drag coefficients. A multicanonical procedure is applied to the two-dimensional Navier-Stokes equation in conjunction with the lattice Boltzmann method to determine the probability distribution functions of the drags generated by a two-dimensional square/rectangular obstacle in quasi-random input flow patterns and for random surface roughness. The results demonstrate that the multicanonical method can estimate the probability distribution function in low-probability regions with far less computational effort than standard techniques.

# Acknowledgements

# Dedication

To my family

# Table of contents

## 5 Drag Probabilities

## 6 Conclusions

## References

# List of Figures

# List of Tables

# List of abbreviations

pdf: probability distribution function

RKIP: Fourier transform based Runge-Kutta interaction procedure

RKHD: 4th order Runge-Kutta method together with a high-order centered finite difference approximation (for the dispersion term)

MC: standard/unbiased Monte Carlo

MCMC: Multicanonical Monte Carlo

# Chapter 1
# Introduction

Section 1.1 will firstly briefly introduce Multicanonical Monte Carlo, as an efficient statistical method for rare events. With such novel statistical method, we focus our research on two typical rare events, rogue waves and (extreme) drags in fluid flows. Sections 1.2 and 1.3 include the research objects, rogue waves and drags in fluid flows. Multicanonical Monte Carlo is developed into two multicanonical procedures for rogue wave probabilities and drag probabilities, which is the main topic of this thesis. Section 1.4 shows the structure of this thesis.

## 1.1 Multicanonical Monte Carlo

The standard/unbiased Monte Carlo procedure that generate probabilities from unbiased random samples, while completely general, by definition samples high probability events far more often than low probability events. Hence to generate the probability density function (pdf) to an accuracy of $10^{-n}$ of the peak value typically $10^{n+2}$ samples are required. Accordingly statistically unlikely but physically important phenomena such as rogue waves cannot be easily studied with such methods.

Biased Monte Carlo methods like Markov Chain Monte Carlo increase the efficiency of sampling in low probability regions. Ideally [1], a Markov chain is generated for which transitions to smaller probability states are always accepted while those to states of larger probability are only accepted with the probability:

$$\min(\frac{pdf(last\_state)}{pdf(new\_state)}, 1) \qquad (1)$$

However, such acceptance rules are somewhat numerically inefficient since the rejected states are not employed in generating the probability distribution functions. Further, the probability distribution function or pdf in (1) is initially unknown.

Accordingly, Multicanonical Monte Carlo was introduced in 1991 by Berg and Neuhus who suggested an iterative pdf updating technique [2] such that the pdf in (1) is initialized as a uniform distribution and subsequently updated after each iteration. This greatly expands the area of configuration space visited by the Markov chain and therefore considerably decreases the sample size required to obtain a smooth pdf in low probability areas. Therefore, these efficient sampling techniques enable the analysis of the pdf in very low probability areas, which cannot be reached in an acceptable time by standard/unbiased Monte Carlo. Moreover, compared to Markov chain Monte Carlo, it is not necessary to find or guess a pdf in Multicanonical Monte Carlo. The updating technique was further improved [3] and smoothing methods applied to improve the determination of the pdfs in very low probability areas [4]. Multicanonical Monte Carlo has subsequently

been applied to numerous fields including optical communication [5][6], optical and oceanic rogue waves [7], and drag probability in fluid flows [8].

## 1.2 Multicanonical procedure for Rogue Wave Probability

The first topic of this thesis involves an extension of the multicanonical procedure to the evaluation of pdfs of waves. In 2016, my supervisor and I developed a multicanonical procedure for evaluating the pdf of rogue wave amplitudes. Rogue waves, which have been extensively studied in e.g. optical systems and deep ocean environments, are waves of extreme height that can be generated or influenced by numerous physical mechanisms, such as odd-order dispersion and nonlinearity. [9][10][11] In our research, the unperturbed or perturbed one-dimensional nonlinear Schrodinger equation adequately describes the interaction between second order dispersion and nonlinearity that leads to rogue wave behavior in many situations and will therefore be employed. The pdf of e.g. the rogue wave heights then still depends on numerous parameters of the initial field such as its average power and spectral half width and is therefore difficult to quantify.

We accordingly introduced a rapid algorithm for evolving the optical field based on a 4th order Runge-Kutta method together with a high-order centered finite difference approximation for the dispersion term that is shown to be generally more efficient than e.g. the Fourier transform based Runge-Kutta interaction procedure of [12]. Distribution functions of wave heights for various input powers and bandwidths are evaluated by employing both the standard/unbiased Monte Carlo and multicanonical sampling. [13] The results of these simulations suggest a simple logarithmic parametrization relating the slope of the pdf to the nonlinearity coefficient in the rogue wave region as well as a greater generation probability for rogue waves in the presence of initial fields dominated by lower frequency components. Additionally, the multicanonical results confirm that under the proper conditions, the oceanic rogue wave probability increases as the nonlinearity is lowered; which appears partially to contradict the accepted belief that nonlinearity generates rogue waves.

## 1.3 Multicanonical procedure for Drag Probability

An object in a fluid flow such as an airfoil in a complex local environment is often deformed through fluid-structure interactions. [14] The resulting variations in the drag and lift coefficients can then influence aircraft design parameters. [14][15] Such deformations are generally either analyzed in isolation [14][15][16] or in the context of optimizing the drag and lift coefficients of the affected structures [17]. However, these analyses generally neglect the pdf of the deformations and therefore cannot predict the reality that an optimized airfoil will actually attain various drags. Even when the statistics of the deformations have been considered, only high probability deformations were examined as a result of the substantial computational time required to perform each realization. [18]

We accordingly present below a multicanonical procedure for evaluating the pdf of drags in fluid flows. Our research demonstrates in a simple test case that, in a similar fashion to the oceanic rogue wave model, the nonlinearity of the two-dimensional Navier-Stokes equation combined with the freedom to deform an object at any set of surface points gives rise to low probability fluctuations with unusually large instantaneous drag coefficients. The numerical analysis integrates the highly efficient multicanonical Monte Carlo statistical

analysis procedure, with a lattice Boltzmann based fluid model. Unlike the standard/unbiased Monte Carlo procedure, which only generates pdfs up to probabilities given by the reciprocal of the number of statistical samples, (**Fig. 6** in [18]) the corresponding bound in the multicanonical Monte Carlo is orders of magnitude lower than this limit. [3][7][13] On the other hand, since the multicanonical procedure employs a Markov chain, additional care must be taken to ensure that the relevant regions of the sample space are appropriately visited.

In particular, the pdf of the drag of a two-dimensional square or rectangular obstacle is evaluated, unlike previous research that primarily calculates or measures the drag for a single realization. [19][20][21] As the numerous computations required to generate an accurate distribution function require considerable resources, the physical parameters and numerical methods must be carefully selected. A comparatively low Reynolds number (~40) ensures that long-time fluctuations and instabilities are absent, and hence that a steady state is attained after a manageable number of time steps. The fluid motion is simulated simply and efficiently with the lattice Boltzmann procedure together with wind tunnel/opening boundary conditions [20][21]. The multicanonical Monte Carlo procedure was then employed to calculate the relevant pdf from a limited number of samples. [3][7][13]

## 1.4 About this thesis

In Chapter 2, after the Multicanonical Monte Carlo is briefly introduced and discussed in section 2.1 the standard models for modeling rogue waves and obstacles in fluid flows are discussed in Sections 2.2 and 2.3.

In Chapter 3, the procedures we developed to implement the multicanonical analysis are introduced together with our propagation method in sections 3.1 and 3.2. These techniques are then further generalized in section 3.3

In Chapter 4, the results of the multicanonical procedure for rogue wave probabilities are presented. The influence of nonlinearity is demonstrated, explained, and confirmed by standard/unbiased Monte Carlo and Multicanonical Monte Carlo results in sections 4.1-4.4. Section 4.5 then verifies the accuracy of the multicanonical results while section 4.6 finally discusses briefly different physical sources of nonlinearity.

In Chapter 5, drag probabilities in fluid flows are included. Section 5.1 contains the results of the multicanonical procedure. Section 5.2 shows the generality of the multicanonical procedure. Section 5.3 verifies the multicanonical procedure. The physics behind the multicanonical procedure is discussed in section 5.4.

In Chapter 6, sections 6.1 and 6.2 respectively conclude the discussion of rogue wave and drag probabilities in fluid flows while section 6.3 presents a summary of our Multicanonical Monte Carlo findings followed by section 6.4, which discusses possible further work on the multicanonical procedure for drag probabilities.

# Chapter 2
# Algorithmic Background

The multicanonical Monte Carlo procedure updates the pdfs after every iteration. The original and the more recent updating methods are discussed here in section 2.1 together with a summary of the Multicanonical Monte Carlo procedure.

To analyze rogue waves, the Nonlinear Schrödinger Equation is often employed to model wave propagation. The dependence of output parameters on the properties of the initial conditions can then be studied by combining several wave components with adjustable relative phases. Since optical and oceanic waves obey the same propagation equation, we are led to a universal multicanonical procedure that predicts rogue wave probabilities in both cases. The details of the modeling method are presented in section 2.2.

To compute drags in fluid flows, the Lattice Boltzmann Model is employed to model the fluid motion while the momentum exchange method is applied to determine the drag coefficient. Section 2.3 briefly introduces this model.

## 2.1 Multicanonical Monte Carlo
2.1.1 General Multicanonical Monte Carlo procedure

The Multicanonical Monte Carlo procedure is based on the Markov Chain Monte Carlo method. A pdf of the variable of interest, $pdf^{i=0}$, is first initialized as a uniform distribution over all possible states of the observed variable. Starting from a random realization of a Markov chain the multicanonical procedure perturb the states of the chain by directly perturbing the like boundary or initial conditions of the observed variable.

In the first iteration, the procedure obtains a certain number of samples by an unbiased Markov Chain Monte Carlo calculation, in which $pdf^{i=0}$ is used as the pdf in (1). Additionally, if the pdf is partially known, $pdf^{i=0}$ can also be a combination of the known part and the unknown part, where $pdf^0(\text{unknown state}) = \dfrac{(1 - \sum pdf^0(\text{known state}))}{\text{Number of known states}}$. During the initial iteration, all sampled states are collected into a histogram, $H^{i=0}$, where the probabilities are given by (1). At the end of the initial iteration, $pdf^0$ will be updated to $pdf^{i=1}$ and $pdf^1$ will be used as the pdf in (1) in the next iteration. All iterations repeat the above procedure until the target distribution, $pdf^{i>1}$, is attained and $pdf^i$ is the result for the desired pdf. In 1991, Berg and Neuhaus gave a simple pdf updating method as:

$$pdf^i(n) = c_n pdf^{i-1}(n) H^i(n) \tag{2}$$

where $i$ is the iteration order, $n$ is the histogram bin number and $H^i$ is the histogram generated in the $i$th iteration. The normalization constant $c$ insures that the histogram elements sum to unity. [2] In 1998, Berg improved his method by introducing recursive weight estimates. The pdf is updated by the following formulas. [3]

$$pdf^i(n) = \frac{pdf^i(n-1)}{pdf^{i-1}(n-1)} pdf^{i-1}(n)(\frac{H^i(n)}{H^i(n-1)})^{G^i(n)} \tag{3}$$

$$G^i(n) = \frac{g^i(n)}{\sum_{l=1}^{i} g^l(n)} \tag{4}$$

$$g^l(n) = \frac{H^l(n-1)H^l(n)}{H^l(n-1)+H^l(n)} \tag{5}$$

However, for this procedure to be compatible with the above pdf updating methods in low probability areas, all state changes must be constrained along a well-defined Markov Chain. This requires that the perturbations of the relevant output variables should be sufficiently small. (See Section 2.1.2.2). Further, the state changes should (ideally) tend towards lower probability areas. The acceptance rule (1) with the initial pdf directs the transitions towards lower probability areas. In this manner, after the first Monte-Carlo iteration, increasingly lower probability areas are sampled. However, in this thesis we observe that the acceptance rule causes the Markov chain to evolve towards less sampled areas that are not necessarily equivalent to low probability areas. This results in systematic errors that lead to local errors in the pdfs. For example, the first initial condition might result a state in a low probability area. At the same time, the small perturbations will push the states out of the low probability area slowly even with the acceptance rule (1). In calculating the probabilities of rogue wave amplitudes, this can lead to oversampling certain low probability areas yielding an artificially large value of the probabilities in the tail regions.

Finally, for small numbers of samples the fluctuations in the low probability areas are large. Here Eq. (2) diverges if the bins of H are initially empty but acquire samples during an iteration. However in Eq. (3), the adjacent bin is included in the updating, reducing the likelihood of an empty bin and smoothing the resulting pdf. Such a smoothing procedure involving averaging over a number of adjacent bins, which was introduced in [4], resulted in significant improvements compared to Berg's original method. [4] However, this improvement results from a theoretical approximation to the weights and the increased smoothness only appears as a side effect. Further, the treatment of the smoothing mechanism in [4] lacks a theoretical analysis. Here we advance the conjecture that the pdfs can be optimally obtained if the sampling method is sufficiently efficient that the updating method can function as intended. Simply ensuring the smoothness of the pdf by averaging over adjacent bins itself leads to systematic errors and may not function properly for pdfs with large second order derivatives.

2.1.2 Multicanonical Monte Carlo Techniques

While Multicanonical Monte Carlo yields the pdf for probabilities far lower than the reciprocals of the sample sizes, the results fluctuate far more than those of the standard Monte-Carlo method. Hence techniques such as setting the values of unsampled histogram bins to unity, the determination of the optimal perturbation size and acceptance rate in the Markov chain, varying the sample sizes of the iterations, and the optimization of the endpoint criterion can significantly improve the multicanonical results.

## 2.1.2.1 Initialization of H

Normally, the values of H are initially set to unity so that empty bins do not invalidate the updating procedure. This enhances the applicability of the procedure to regions of small pdf in which the histogram bins are sparsely sampled in a single iteration, but at the cost of systematic errors. Indeed, in the calculations of this thesis, these systematic errors only vanished when the bin was instead initialized to zero. However such a procedure requires that each steps in the Markov chain only slightly affects the output variables of interest. Such a condition is however unfortunately found here to be violated in a system close to chaos. However, if the computational resources are sufficient to allow a sample size that far exceeds the total number of bins, the errors are small when the bins are initialized to unity, which is therefore suggested when analyzing systems close to chaos.

## 2.1.2.2 Optimal perturbation size and acceptance rate

The size of the perturbations between successive states of the Markov chain is of particular importance for small sample sizes. In particular, for the Markov chain to be meaningful, the perturbation cannot be excessively large, but if the perturbation is instead too small all samples may fall into a limited region leading in most cases to a completely incorrect pdf. To find the optimal step size however requires in general an empirical study of the effects of varying the input parameters. Similarly, since the number of realizations that fall into previously unsampled regions decreases with iteration number, the acceptance rate is often monitored and the perturbation size adjusted accordingly to insure that a nearly constant fraction of proposals are accepted. Unfortunately to our knowledge no theoretical studies of the optimal acceptance rate appear to exist and any optimization procedure would therefore again be empirical. Additionally, adjusting the step size generally proves difficult for a small number of iterations.

## 2.1.2.3 Iteration sample sizes

The density of realizations in the rare probability regions can also be enhanced by increasing the number of samples in successive iterations. However a sufficiently large sample size is still required in the first iteration.

## 2.1.2.4 Stopping criterion

There are two widely employed stopping criteria for the Multicanonical Monte Carlo method. One of these ends the iteration when the intermediate histogram is constant to within a certain factor. The second procedure does not terminate the entire calculation until the pdf agrees with that of the previous iteration to a certain accuracy.

While the multicanonical method provides a simple procedure for determining the pdf in rare probability regions, it is important to note that the accuracy of the result is not simply established. As well, unlike in for example transition matrix formulations, no information is obtained from rejected states, which affects the overall efficiency of the method [22].

## 2.2 Modeling of wave propagation
2.2.1 Physical model of rogue waves

Rogue wave propagation is commonly modeled with the one-dimensional nonlinear Schrodinger equation in which the time and space variables are scaled differently in optical and ocean contexts. It should be remarked that although the nonlinear Schrodinger equation coincides Schrodinger equation in quantum physics in form, it represents a wave propagation influenced by the effects of dispersion and nonlinearity, which has the totally different physics meaning from Schrodinger equation's in quantum physics. In optics, in terms of the complex field $A(z,t)$, which is periodic over the computational window (CW) length, this equation, which preserves the power $|A|^2$ integrated over the computational window, is given by [14]

$$\frac{\partial A}{\partial z} = i\frac{1}{2}\frac{\partial^2 A}{\partial t^2} + \beta_3 \frac{\partial^3 A}{\partial t^3} + i\gamma |A|^2 A \tag{6}$$

where the distance, time and computational window variables are given in **Table. 1**. The nonlinear Schrodinger equation is then obtained by setting the third order dispersion coefficient, $\beta_3$, to 0.

In ocean contexts for which third order dispersion is typically neglected, the scaling is instead performed as in **Table. 1** according to [15], where $\omega_0$ represents the carrier frequency, $k_0 = \omega_0^2 / g$ is the wavenumber, $\Delta\omega$ is the half width of the frequency spectrum of the field and the scale factor is given in terms of the oceanic signal duration (OCD) by $\upsilon = CW / (OCD \cdot \Delta\omega)$,

**Table. 1**: Parameter Scaling

| | Scaled $z$, $z'$ | Unit of z | Scaled $t$, $t'$ | Unit of t | Scaled $A$, $A'$ | Unit of $A$ |
|---|---|---|---|---|---|---|
| Optical | $\frac{1}{1.04} km^{-1} \cdot z$ | km | $\frac{1}{2} ps^{-1} \cdot t$ | ps | $\sqrt{\frac{52}{5\gamma}}\frac{1}{10}\sqrt{W^{-1}} \cdot A$ | $\sqrt{W}$ |
| Oceanic | $2k_0 \left(\frac{\upsilon \cdot \Delta\omega}{\omega_0}\right)^2 \cdot z$ | m | $\upsilon \cdot \Delta\omega \cdot t$ | s | $\frac{k_0 \omega_0}{\upsilon\Delta\omega\sqrt{2\gamma}} \cdot A$ | m |

In the optical calculations, the propagation length and signal duration are set to 7.69km and 102.4ps. Different values of the initial power are modeled by appropriately scaling $\gamma$. In the oceanic case, the propagation length and oceanic signal duration equal 3.46km and

7

480s. In both cases, the propagation length and signal duration correspond to a scaled propagation length $z' = 8$ while the computational window widths $t'$ is set to 51.2, the integral of $|A'|^2$ over the computational window equals 256 and the third order dispersion term is omitted.

2.2.2 Initialization and measurement

In the optical context, we first elucidate several general properties of the distribution function by considering an initial field described by the sum of ten monochromatic waves according to

$$A(z = 0, t) = \sqrt{\frac{5\gamma}{52}} 10\sqrt{W} \sum_{n=1}^{10} \cos(\omega_n t + \varphi_n) \tag{7}$$

$$A(z = 0, t) = \sqrt{\frac{5\gamma}{52}} 10\sqrt{W} \sum_{n=11}^{20} \cos(\omega_n t + \varphi_n) \tag{8}$$

with frequencies, $\omega_n = \frac{2\pi}{CW} \cdot n$. We then employ the multicanonical procedure in [18] to determine the pdf of the scaled wave power at a fixed point in the computational window, $|A(z = 8, t = 0)|^2$ or the pdf of the maximum of the scaled wave power in the computational window, $\max_{t \in CW} |A(z = 8, t)|^2$, after a propagation distance of $z = 8$ scaled distance units. The Markov chain in these calculations is composed of the 10 (9 in calculations that employ periodic boundary conditions) phase variables of (7). The magnitude of the variations in the phase variables between successive iterations is chosen such that the results are both in optimal agreement with those of the standard/unbiased Monte Carlo method in the high probability region and are nearly invariant when this magnitude is changed slightly in the low probability regions. To attain a statistically invariant steady-state distribution, the nonlinear Schrodinger equation was employed to propagate the field beyond five soliton periods ($2.5\pi$) [23] and the wave power was then sampled at $z = 8$, following a procedure often applied in oceanic propagation.

In oceanic propagation, we instead employ the Joint North Sea Wave Project spectrum (JNSWP) ((2) in [24], p160) to construct an field with the energy spectrum

$$E(f) = \alpha g^2 (2\pi)^{-4} f^{-5} \exp\left[ -\frac{5}{4} \left( \frac{f}{f_{peak}} \right)^{-4} \right] \chi^{\exp\left[ -\frac{1}{2} \left( \frac{f - f_{peak}}{\sigma f_{peak}} \right)^2 \right]} \tag{9}$$

where $\alpha = 0.0081$, $g = 9.832 m \cdot s^{-2}$, $f$ represents the frequency scaled according to $f' = \frac{f}{\upsilon \cdot \Delta\omega}$ with $\Delta\omega$ the half width at half the maximum value $E(f_{peak})$ of (9), and

$f_{peak} = 0.1 Hz$, $\sigma = 0.07$ for $f \le f_{peak}$ and 0.09 otherwise and $\chi$ denotes a scalar constant that determines the value of $\Delta\omega$ according to the formulas in [10]. Expressing the surface elevation as

$$\xi(z,t) = \text{Re}\left[ A(z,t) \cdot \exp(i2\pi f_{peak} t) \right] \tag{10}$$

the initial surface elevation is given by [10]

$$\xi(0,t) := \text{Re}\left[ A(0,t) \cdot \exp(i2\pi f_{peak} t) \right]$$

$$= \sum_{n=1}^{500} \sqrt{2E(f_n)\Delta f} \, \cos(2\pi f_n t + \varphi_n)$$

$$= \sum_{n=1}^{500} \sqrt{2E(f_n)\Delta f} \, \cos(2\pi f_n t + \varphi_n) \exp(-i2\pi f_{peak} t) \exp(i2\pi f_{peak} t)$$

which yields for the corresponding field

$$A(0,t) = \sum_{n=1}^{500} \sqrt{2E(f_n)\Delta f} \, \cos(2\pi f_n t + \varphi_n) \exp(-i2\pi f_{peak} t) \tag{11}$$

with $\Delta f = \dfrac{1}{OCD}$ and phase terms $\varphi_n$ that are randomly distributed in $[0, 2\pi]$. Note that since the nonlinear Schrödinger equation conserves the energy over the oceanic signal duration and $E(f) \propto \alpha$, changing $\gamma$ in (6) is equivalent to varying $\alpha$, which enters implicitly in (11).

In the calculations of oceanic waves, each field realization is propagated 8 units in $z$ and the quantity $\xi(z = 8, t) = \text{Re}\left[ A(z = 8, t) \cdot \exp(i2\pi f_{peak} t) \right]$ is evaluated. The wave height is defined as the maximum magnitude of the wave displacement, c.f. **Fig. 3.2** in [24]. If a given point in the computational window is specified, its "relative wave height" is defined as the difference in magnitude of the field at this point and the smaller of the minima situated immediately to the left and the right of the point. A rogue wave corresponds to a wave with a height larger than 2.2 times the significant wave height, which is given in terms of the energy spectrum $E(f)$ by [24]

$$\text{significant wave height} \approx 4.0\sqrt{\int E(f)\,df} \approx 4.0\sqrt{\sum_{n=1}^{500} E(f_n)\Delta f} \tag{12}$$

so that the square of the scaled minimum rogue wave height, defined as 2.2 times of significant wave height, varies as the scaled wave energy. Since nonlinearity affects the field spectrum, the magnitude of the significant wave height depends on the computational parameters. With these conventions, the percentage of rogue waves, the pdf of the square

9

of the scaled wave heights, the pdf of the maximum of the square of scaled wave heights and the pdf of the relative wave heights at a specified position can be determined.

In oceanic wave contexts, from **Fig. 1** of [24] increasing $\chi$ both lowers $\Delta\omega$ and raises the total energy integrated over the oceanic signal duration. However, when $\chi$ is specified within an interval such as $[3,8]$ in [24], as $v \cdot \Delta\omega$ is held constant, the definitions in **Table. 1** insure that the energy within the oceanic signal duration does not vary with $\chi$. Since the percentage of rogue waves is obtained from the surface elevations over the same oceanic signal duration after a fixed propagation length, the percentage of rogue waves, the pdf of the square of the wave heights and the pdf of the square of the maximum wave heights are obtained from samples with equal energies over the oceanic signal duration but different $\Delta\omega$. As $v \cdot \Delta\omega$ is also held constant when examining the effect of varying $\gamma$, the initial conditions for the percentage of rogue waves, the pdf of the squares of the wave height and the pdf of the squares of the maximum wave heights in such calculations possess the same $\Delta\omega$ but different energy over the oceanic signal duration.

### 2.3 Modeling of obstacles in fluid flows

The lattice Boltzmann method represents a fluid by a continuous particle distribution function that is defined [20] on a discrete set of constant velocities, $c_i$, lattice points, $\mathbf{x}$, and times, $t$,

$$f_i(\mathbf{x},t) := f(\mathbf{c}_i,\mathbf{x},t) \tag{13}$$

such that the fluid density is given by

$$\rho(\mathbf{x},t) = \sum_i f_i(\mathbf{x},t) \tag{14}$$

The research here employs the D2Q9 velocity set in a two-dimensional space, normalized according to [25][26][27] for which the sound speed $c_s = 1/\sqrt{3}$ is given by

$$\mathbf{c}_i \in \left\{(1,0),(1,1),(0,1),(-1,1),(-1,0),(-1,-1),(0,-1),(1,-1),(0,0)\right\} \tag{15}$$

The particle distribution function is then evolved in time according to

$$f_i(\mathbf{x}+\mathbf{c}_i t, t+\Delta t) = f_i(\mathbf{x},t) + \Omega_i \tag{16}$$

which can be implemented as two separate numerical steps that conceptually correspond to particle collision and propagation. The nonlinear BGK collision operator implements the first of these steps according to

$$\Omega_i = -\frac{1}{\tau}\left(f_i(\mathbf{x},t) - f_i^{eq}(\mathbf{x},t)\right) \tag{17}$$

$$f_i^{eq}(\mathbf{x},t) = \rho\omega_i\left[1 + 3(\mathbf{c}_i \cdot \mathbf{u}) + \frac{9}{2}(\mathbf{c}_i \cdot \mathbf{u})^2 - \frac{3}{2}(\mathbf{u} \cdot \mathbf{u})\right] \tag{18}$$

with weights

$$\omega_i \in \left\{\frac{1}{9}, \frac{1}{36}, \frac{1}{9}, \frac{1}{36}, \frac{1}{9}, \frac{1}{36}, \frac{1}{9}, \frac{1}{36}, \frac{4}{9}\right\} \tag{19}$$

(18) and (19) are derived from the Hermite series expansion of the Maxwell-Boltzmann distribution function for a system with velocity **u** by neglecting terms of greater than second order and applying an appropriate finite difference stencil. This procedure conserves mass, momentum and energy. [27] The kinematic viscosity in this model equals

$$\upsilon = c_s^2\left(\tau - 1/2\right) \tag{20}$$

Accordingly, the particle distribution function after collision is given by

$$f_i^*(\mathbf{x},t) = f_i(\mathbf{x},t) - \frac{1}{\tau}\left(f_i(\mathbf{x},t) - f_i^{eq}(\mathbf{x},t)\right) \tag{21}$$

after which the distribution functions are evolved in time according to (16)

$$f_i(\mathbf{x} + \mathbf{c}_i t, t + \Delta t) = f_i^*(\mathbf{x},t) \tag{22}$$

The longitudinal *x*-component of the drag, which replaces the wave height in [7] as the relevant physical quantity, is evaluated with the momentum exchange method [19], namely

$$Drag = \left(\sum_{i\in\{1,2,8\}} f_i(\mathbf{x},t+\Delta t) - \sum_{j\in\{5,6,4\}} f_j(\mathbf{x},t+\Delta t)\right) - \left(\sum_{k\in\{1,2,8\}} f_k(\mathbf{x},t) - \sum_{l\in\{5,6,4\}} f_l(\mathbf{x},t)\right) \tag{23}$$

$\mathbf{x} \in$ obstacle surface

The steady state drag was computed from the above sums after the waves reflected from the boundary points were attenuated which occurs after a certain propagation time, as evident from **Figs. 4** and **6**. In all the above formulas, normalized units are employed in accordance with the standard lattice Boltzmann prescription. [26]

# Chapter 3
# Numerical Methods

To provide samples sufficiently efficiently to enable Multicanonical Monte Carlo analyses of fluctuations in fluid motion, in the first section of this chapter the RKHD is described and tested. The multicanonical procedure here applies to both optical and oceanic rogue wave probabilities as a result of the similarity between optical wave propagation and oceanic wave propagation.

To study the effect of the surface boundary on the drag the boundary conditions of the Lattice Boltzmann model introduced in Chapter 2 are perturbed in Section 3.2 to provide random samples of different drags to the Multicanonical Monte Carlo analysis. The independence of the results on the numerical grid is also verified in this section.

## 3.1 Multicanonical procedure for rogue wave probability
3.1.1 Improved Wave propagation method: RKHD

The nonlinear Schrodinger equation is often solved with FFT (Pseudo-spectral) methods, [9][10][12] for which the derivatives in the nth order dispersion term are evaluated according to

$$\frac{\partial^n A}{\partial t^n} \approx FFT^{-1}\left\{(i\omega)^n FFT\left[A(z,t)\right]\right\} \tag{24}$$

However, while (24) can be employed to reduce the error in $t$ for periodic fields to machine precision, the small step length $\Delta z$ required, especially in the case of large nonlinearity, can result in unacceptably long computation times for an insufficient number of transverse grid points. Therefore, a $l$th order $O(\Delta t^{2l})$ central difference approximation

$$\frac{1}{2!}\frac{\partial^2 A}{\partial t^2} = \frac{1}{2!}\frac{1}{\Delta t^2}\sum_{j=-6}^{j=6} c_{2j} A(t_{n+j}) + O(\Delta t^{12}) \tag{25}$$

is instead employed below, where the $c_{ij}$ are constant coefficients obtained from the *Mathematica* codes in [25]. For N=1024 and $l$=6, $\Delta t = \dfrac{CW}{N} = 0.05$ yielding an $O(\Delta t^{12} \approx 2.44\times10^{-16})$ error, comparable to the accuracy of the FFT method. A single time step then requires $O(N(2\cdot l+1) = 1024\cdot13)$ real operations with the central difference method and $O(2N\log_2(N) = 1024\cdot20)$ complex operations for the FFT procedure. The $z$ propagation is performed with the $O(\Delta z^4)$ Runge-Kutta method without the interaction representation of [12] according to the standard formula.

$$k(z,A) = i \cdot \frac{1}{2!} \frac{1}{\Delta t^2} \sum_{j=-6}^{j=6} c_{2j} A(t_{n+j}) + i\gamma |A|^2 A$$

$$k_1 = k(z_n, A(z_n))$$

$$k_2 = k(z_n + \frac{\Delta z}{2}, A(z_n) + \frac{\Delta z}{2} k_1)$$

$$k_3 = k(z_n + \frac{\Delta z}{2}, A(z_n) + \frac{\Delta z}{2} k_2)$$

$$k_4 = k(z_n + \Delta z, A(z_n) + hk_3)$$

$$A(z_{n+1}) = A(z_n) + \frac{\Delta z}{6}(k_1 + 2k_2 + 2k_3 + k_4) \tag{26}$$

where $\Delta z$ is set to a value slightly below the stability limit, which varies as $(\Delta t)^\alpha$ where $\alpha$ denotes the dispersion order. [26, p.96]  Since most of our calculations require a number of transverse grid points, N, between 1024 and 1440, our comparisons of the RKHD and RKIP are further performed with N in this range.

To illustrate, in **Fig. 1**, we calculate the error

$$\frac{\sum_0^{1023} \left| |A(z = 80, t_n)|^2 - |A\_exact(z = 80, t_n)|^2 \right|}{Max_{n \in [0,1023]}\{|A\_exact(z = 80, t_n)|^2\}} \tag{27}$$

for 5th and 7th order accurate procedures and a second-order soliton input field with $\gamma = 1$. Here the stability limit for N=1024, namely $\Delta z \le 0.00195122$, coincides with the rightmost points of the curves of RKHD while the computation was performed for 40,000, 41,000, 50,000, 100,000 and 200,000 propagation steps.
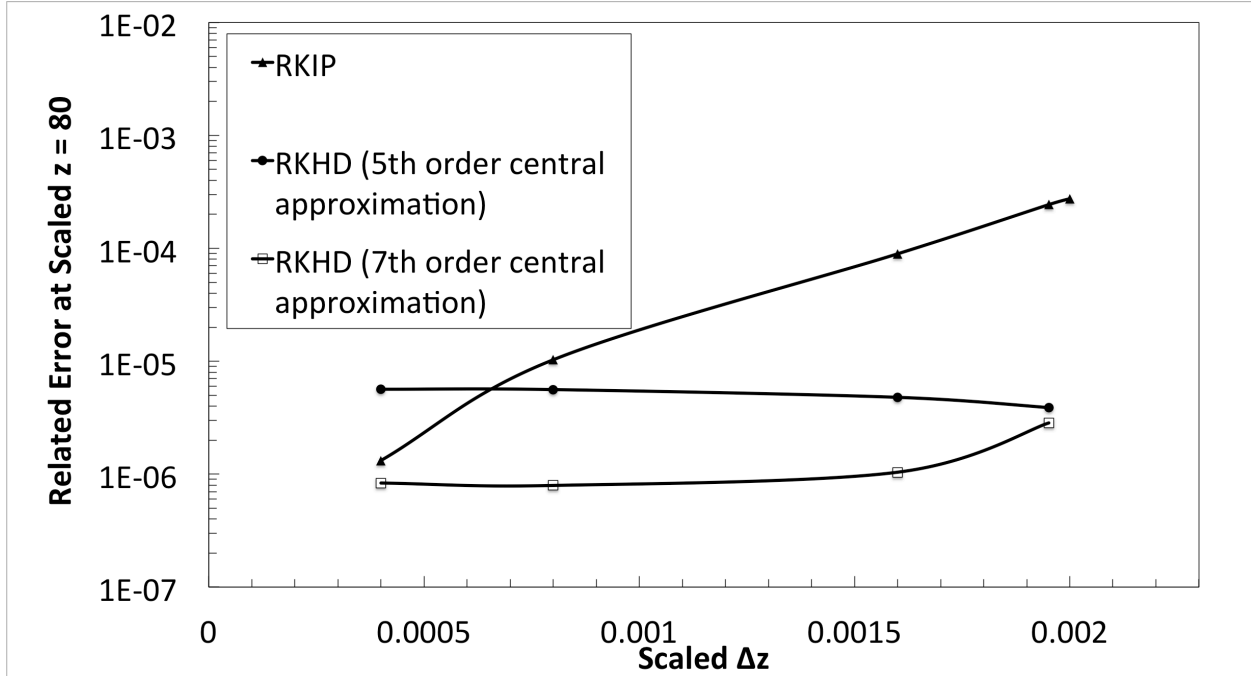
**Figure. 1**: The accuracy of the RKHD and RKIP methods.

Evidently, the RKHD method displays the greatest efficiency, as for $l = 7$ and $\Delta t = 0.03$ the magnitude of the error of the central difference approximation already attains machine precision while for long propagation distances the procedure is both more stable and accurate than the RKIP. Hence while the RKHD accurately propagates a fifth order soliton $10^6$ steps corresponding to 40 soliton periods ($20\pi$) with $\Delta t = 0.025$ in 83s, performing the identical calculation with the RKIP requires 157s and diverges when z ~ 25. However, to evolve input fields with wider frequency spectra the transverse grid point spacing must be reduced.

The oceanic excitation (11) possesses far higher frequencies than the lowest 20 periodic frequencies in the computational window that enter into (7) and (8). Consequently, in our calculations, when $\chi = 8$ and $\gamma = 0.15$, the RKIP requires a minimum of 2048 grid points to achieve acceptable accuracy while the RKHD attains a similar level of precision for 1440 grid points. However, the RKHD generally is found to be less efficient for higher frequency excitations.
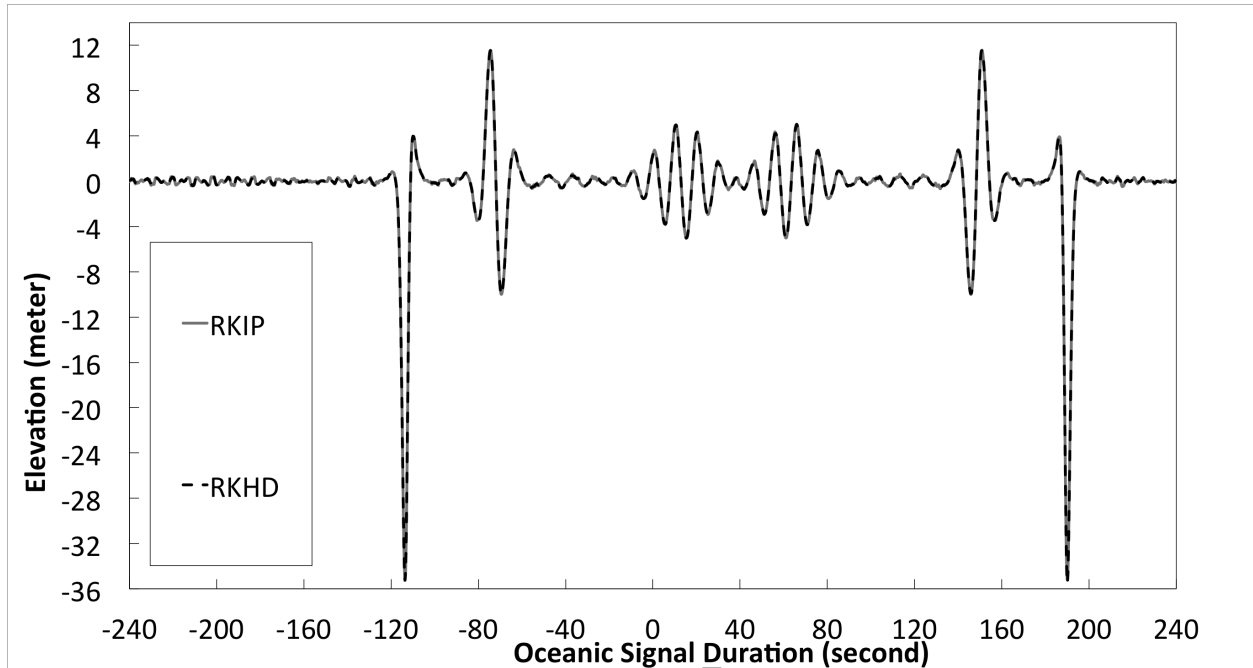
**Figure. 2**:  The field obtained after propagating (11) with equal phases with the RKIP and RKHD.

Below, the RKIP is first employed with (11) for equal phases as the initial field and subsequently the RKHD parameters that produce a result of equivalent accuracy are determined, c.f. **Fig. 2** which plots the field after 40000 propagation steps of length for $\gamma = 0.15$ and $\chi = 8$ for both methods where the minimum rogue wave height equals 34.6m (Hence in this state, any wave whose wave height larger than 34.6m is a rogue wave. i.e. the wave near oceanic signal duration = -120s).  Evidently in this calculation the RKHD performs better than the RKIP as fast Fourier transforms are absent in the RKHD and hence a 1440 points grid yields equivalent precision to a 2048 points RKIP implementation.

### 3.1.2 Modifications for the multicanonical procedure

A slight modification of the standard multicanonical method of e.g. [13] will be employed to determine the pdf of rogue waves.  In particular, if the magnitude, $\varepsilon$, of the parameter change between the Markov chains associated with two successive realizations is too small, states in a restricted region of phase space are oversampled while as $\varepsilon \to \infty$ the method reverts to the standard Monte-Carlo approach, limiting the probability region that can be sampled.  As well, for large $\gamma$ the probability of high energy fluctuations increases so that additional realizations are required to evenly sample the histogram bins.  Increasing the bin width ameliorates this problem at the cost of additional truncation error. [13] Hence in the calculations here, $\varepsilon$ is adjusted after each iteration with the objective of achieving an acceptance rate of $\approx 30\%$ for the subsequent iteration. Further, in the lowest probability regions, to avoid unsampled histogram bins which can lead to a fictitious increase in the pdf at the edges of the distribution that is not removed by further iterations, the number of realizations at large iteration number is increased and unity is added to the intermediate histogram elements during the calculation in [13] (except where noted).

15

## 3.2 Multicanonical procedure for drag probability

3.2.1 Multicanonical procedure

To decrease the computation time required to accumulate a sufficient number of statistical samples, the multicanonical Monte Carlo biased sampling procedure is employed. In the same manner as in the previous analysis of the pdf of oceanic rogue wave heights, variations of the input fluid velocities are incorporated by superimposing multiple waves with a fixed spectrum of frequencies but with random amplitudes and phases. [23] Shape fluctuations of the obstacle are modeled by displacing its boundary outward by one grid point over a varying number of surface points.

The multicanonical procedure is, however, only acceptably accurate if the variations of the input conditions or the surface profile over a single Markov step as well as the histogram bin size satisfy certain constraints. The magnitude of the variation must ensure that the average difference in the results of two successive Markov chain realizations varies smoothly and constitutes a significant fraction of the histogram bin size. Since the largest final state changes generally occur for the lowest probability states, the initial or boundary conditions that generate the lowest probability states were first inferred. Subsequently, the perturbation size was set such that for these states a Markov step resulted in an average displacement of 1-3 histogram bins, as discussed further in conjunction with **Figs.19** and **20**.

The pdf bin size must both be larger than the intrinsic accuracy of the lattice Boltzmann method which here determines the drag to $\approx 10^{-3}$ and must ensure that the number of samples varies relatively smoothly between adjacent bins. Excessive bin sizes however decrease the number of transitions among the bins and hence degrade efficiency. Here a representative calculation was repeated for several bin widths after which a size of 0.005 was selected for the calculations, which employed 33677 and 47219 Markov steps.

The drag calculations were performed on an evenly spaced $50 \times 60$ point ($x,y$) grid. A constant speed left boundary and a unit density right boundary implemented according to the procedure of Zou and He [21] were employed along the $x$-direction while periodic boundary conditions were implemented in the $y$- direction and the bounce back condition was applied to obstacle points. [26][27] The relaxation time $\tau = 0.6$, and the particle distribution functions were initially set to $f_i(\mathbf{x},t) = 1/9$, at each fluid point, corresponding to unit density and zero velocity, together with $f_i(\mathbf{x},t) = 0$ at each obstacle point.

To illustrate the efficiency and accuracy of our computational procedure, the pdf of the drag is calculated below for two types of perturbations. The first of these, illustrated in **Fig. 3,** superimposes the lowest four periodic sinusoidal plane waves along the input axis at

$x = 1$ according to $u_x(x = 1, y \in \{1, 2, ...60\}) = 0.05 \sum_{n=1}^{4} \sin(\frac{2\pi n}{60} y + \varphi_n)$ , where $\varphi_{n \in \{1,2,3,4\}}$ are

random but uniformly distributed phases over $[0, 2\pi)$. The drag was then evaluated over a centered square obstacle extending over 10 points $\times$ 10 points and located twenty grid points downstream from the left boundary. The multicanonical procedure was implemented by perturbing a randomly selected phase at the beginning of each realization

in exactly the same manner as in [7] while the drag was evaluated after each phase change by performing 10,000 lattice Boltzmann time steps in order to arrive at a steady-state quantity, as illustrated in **Fig. 4**. The procedure in [26] was employed to verify the validity of the above parameter choices.

In the second calculation, depicted in **Fig. 5**, the input velocity was set to 0.12 but the upper and lower surfaces of the obstacle were modified between successive multicanonical realizations by converting a randomly selected grid point directly above the surface from a fluid to an obstacle or an obstacle to a fluid point. The dimension of the initial obstacle in this calculation equals $N_x \times N_y = 20 \times 10$ grid points and is situated fifteen points away from the inlet. The drag after each step in the Markov chain was associated with the steady-state value after 20,000 lattice Boltzmann time steps, c.f. **Fig. 6**. These problem and computational grid parameters are motivated by the standard test calculations of e.g. [27]. Further, for a larger number of grid points the normalized time required to generate the steady state value of the drag is greatly increased. For example for $98 \times 120$ grid points and an obstacle of size $40 \times 20$, a steady state distribution is only obtained after at least $\sim 10^5$ normalized time units.



**Drag = 0.0041305**
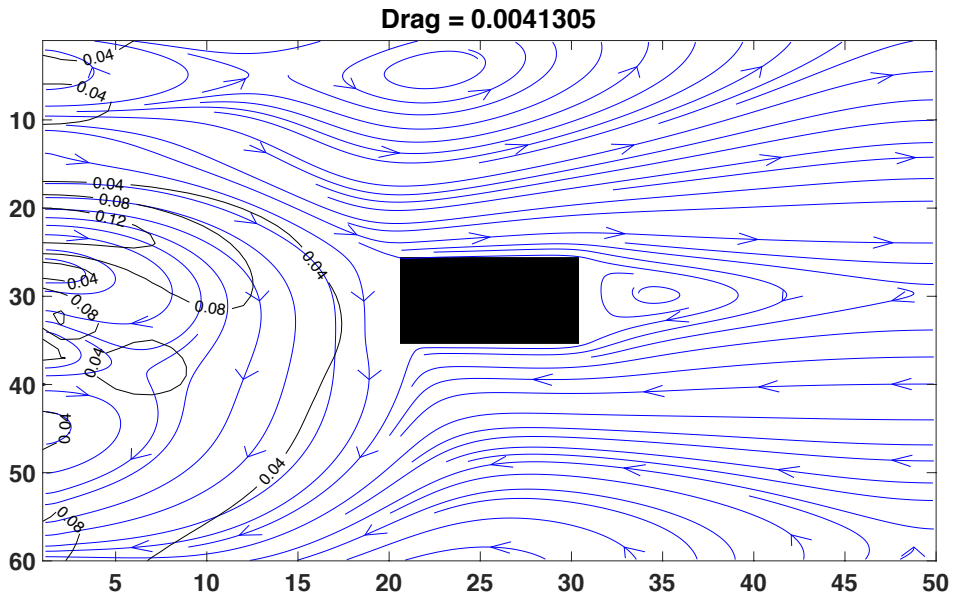
**Figure. 3** The steady state achieved after 20,000 time steps for a particular realization of the sum of four-plane-wave input velocity perturbation. The contour lines indicate fluid velocities while the arrows indicate the flow direction.
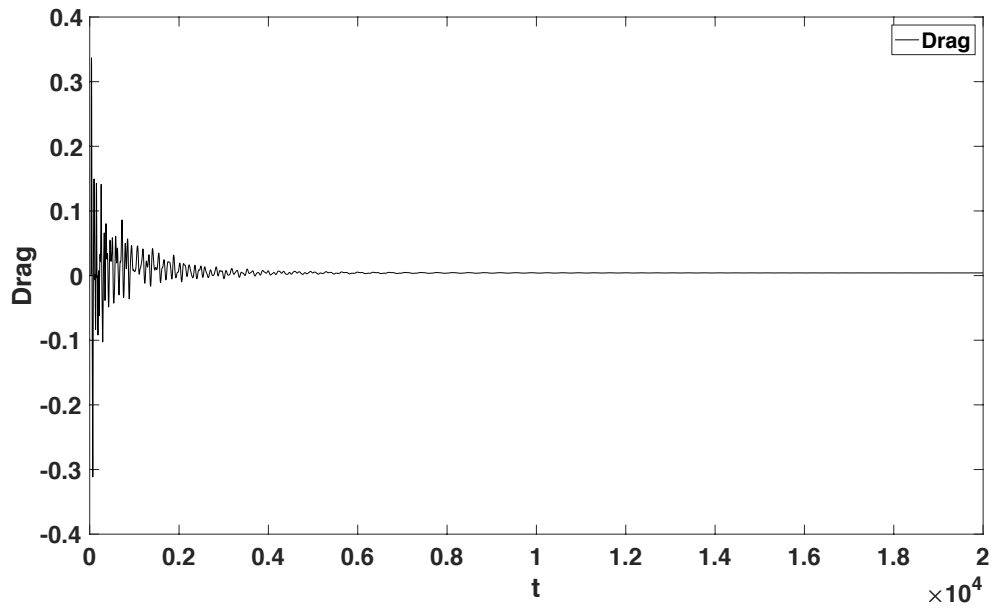
**Figure. 4** The drag as a function of time for the calculation of **Fig. 3**. Since in this case the transient oscillations associated with the initial conditions are effectively absent after 10,000 time steps, drag values are computed after this number of time steps.
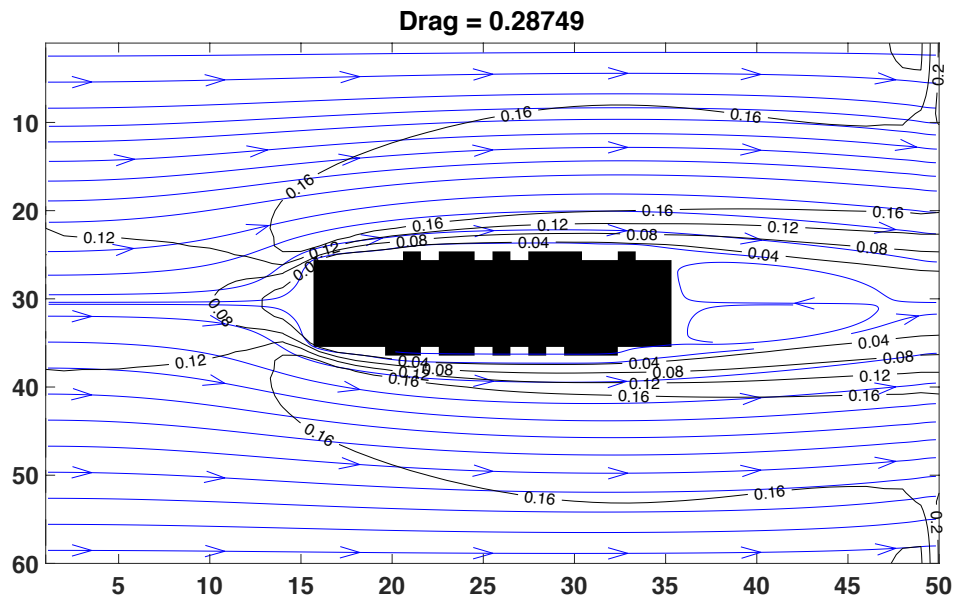


**Figure. 5** As in **Fig. 3** but for 30,000 time steps for a particular realization of a distorted rectangular obstacle.
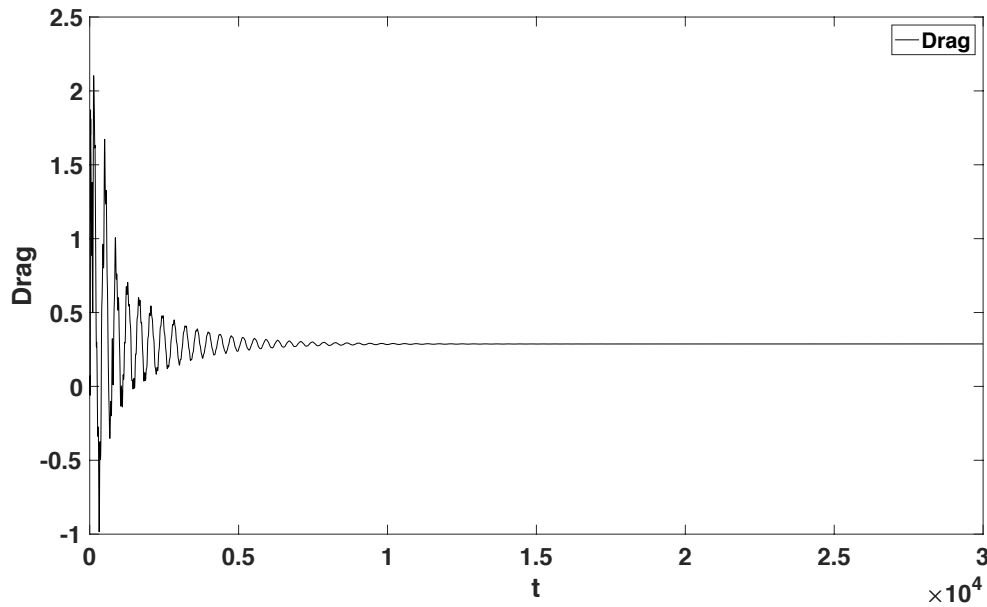
**Figure. 6** As in **Fig. 4** but for the realization of **Fig. 5**. Since the required steady state value is only attained after 20,000 time steps, here drag values are computed after this number of time steps.

### 3.2.2 Generalization of modeling

A disadvantage of the small computational grid dimension, however, is that the proximity of the boundary to the obstacle slightly increases the computed drag coefficient. Further, the Zou and He boundary conditions possess an effective width of one grid point spacing and therefore are less effective if the distance between grid point is reduced.

To illustrate the above, the drag of the unperturbed obstacle was computed for grid sizes of $50 \times 60$, $98 \times 120$ and $146 \times 180$. After correcting the latter two calculations by subtracting 0.0332 to account for the influence of the boundary in the smallest $50 \times 60$ computational window, the drag values agree for the different resolutions to within 1% as evident from **Table.2**. If the space from the inlet and outlet boundaries to the obstacle is doubled the boundary effect correction value becomes 0.0143 indicating that the difference in resolution contributes $0.0023 / 0.2291 \approx 1.00\%$ to the difference in the drag. Based on these considerations, a $50 \times 60$ point grid is employed in the subsequent calculations. Since increasing the resolution corresponds to reducing the time step for a fixed Reynolds number, resolution independence is equivalent to temporal convergence in this model.

**Table. 2**

| Resolution | Obstacle | Inlet to Obstacle Distance | Obstacle to Outlet Distance | Drag in the steady state | Boundary Effect Correction | Corrected Drag |
|---|---|---|---|---|---|---|
| $50 \times 60$ | $20 \times 10$ | 14 | 14 | 0.2628 | 0.0332 | 0.2628 |
| $98 \times 120$ | $40 \times 20$ | 28 | 28 | 0.2296 | | 0.2628 |
| $146 \times 180$ | $60 \times 30$ | 42 | 42 | **0.2291** | | 0.2623 |
| $78 \times 60$ | $20 \times 10$ | 28 | 28 | 0.2126 | 0.0143 | 0.2126 |

19

| 154×120 | 40×20 | 56 | 56 | 0.1983 | | 0.2126 |
|---------|-------|-----|-----|--------|--|--------|
| 230×180 | 60×30 | 84 | 84 | 0.1974 | | 0.2119 |
| Difference of drags caused by difference of Resolutions | | | | 0.0332/**2**-0.0143 = **0.0023** ~1.00% | | |

# Chapter 4
# Nonlinearity and Oceanic Rogue Waves

In this chapter, we first demonstrate both quantitatively and qualitatively in Sections 4.1 and 4.2 that in both optical and oceanic contexts, nonlinearity and lower-frequency wave components lead to the amplification of rogue waves. Here the standard unbiased Monte Carlo procedure is insufficient to demonstrate the full range of rogue wave properties. Subsequently the Multicanonical Monte Carlo procedure of Chapters 2 and 3 are applied in Sections 4.3 and 4.4, to verify the qualitative discussions and Monte-Carlo analyses of Sections 4.1 and 4.2. Here the multicanonical pdfs include waves that are much higher and rarer than the typically examined rogue waves. Since many theoretical probability predictions are inaccurate in such low probability areas, section 4.5 justifies the multicanonical results by comparing to those of the standard/unbiased Monte Carlo method. Finally in Section 4.6 the multicanonical procedure is employed to analyze some unusual rogue wave behavior associated with nonlinear effects.

## 4.1 Monte Carlo analysis of wave power
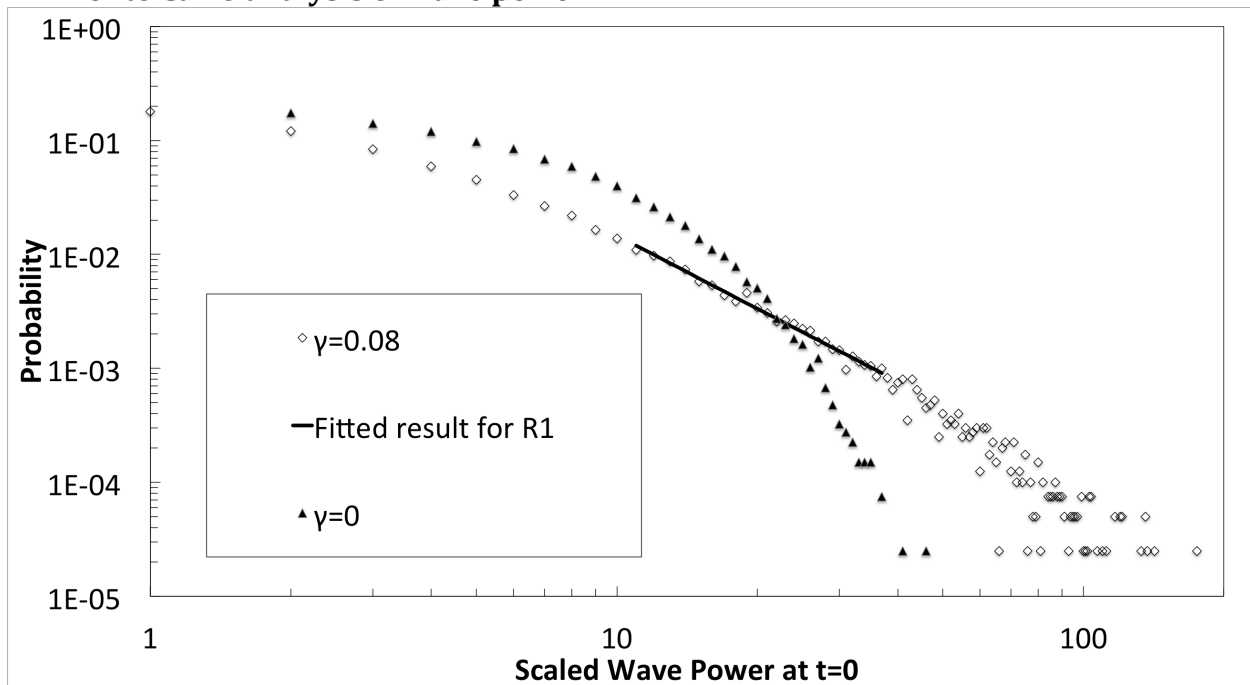


**Figure. 7**: The pdf of the scaled wave power for initial excitations consisting of sums of periodic waves with random phases for two values of the nonlinearity parameter.

Considering first a 40,000 Monte-Carlo evaluation of the pdf of the rogue wave height at $t = 0$ and the excitation of (7), a scaled propagation distance, 8, and a computational window, 51.2, in which the phases are chosen randomly in each realization, a representative result for the pdf of scaled wave power after propagation is displayed in **Fig.**

**7**.   The RKHD is employed with 250 propagation steps and 256 grid points for $\gamma = 0$ (triangle markers) and 2640 propagation steps and 800 grid points for $\gamma = 0.08$ (diamond markers).  As expected, larger values of the nonlinearity coefficient yield a greater rogue wave probability while for probabilities in the interval $[0.001, 0.01]$ the logarithm of the pdf depends nearly linearly on the logarithm of the wave height. In this region, for $\gamma \in [0.001, 0.2]$, a least squares fit to a straight line yields a correlation coefficient $r^2 \geq 0.9662$, with a slope designated $R1$ below; that is, the probability of a given scaled wave power, $P$, varies approximately as $1.9265 \cdot P^{R1}$ with $R1 = -2.121$ where the correlation coefficient $r^2 = 0.9853$ for the curve fit displayed in **Fig. 7**.
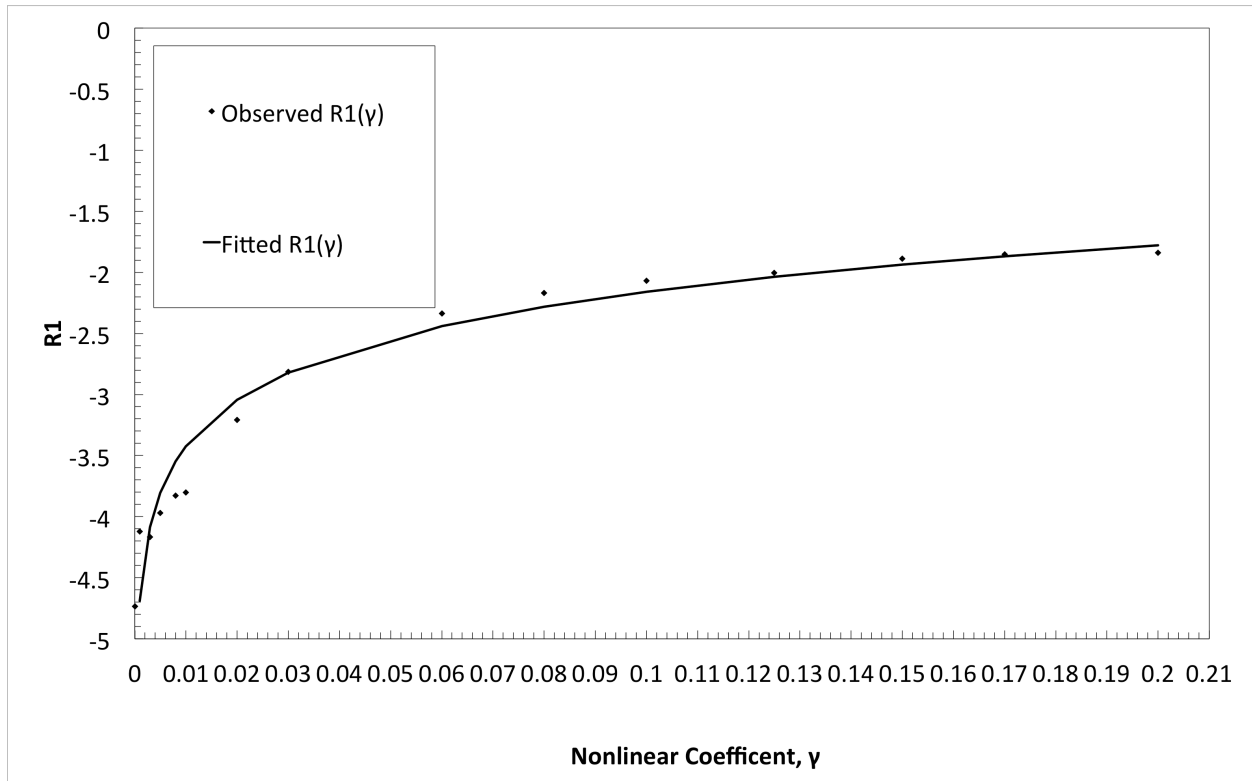


**Figure. 8**: The slope of the pdf as a function of the nonlinear coefficient, $\gamma$ for the RKHD parameters given in **Table. 3**.

**Table. 3**

| $\gamma(0.01)$ | 0 | 0.1 | 0.3 | 0.5 | 0.8 | 1 | 2 | 3 | 6 | 8 | 10 | 12.5 | 15 | 17 | 20 |
|---|---|---|---|---|---|---|---|---|---|---|---|---|---|---|---|
| Number of propagation steps | 250 | | | | | | | | 2560 | 2640 | 4000 | 8000 | 8000 | 16000 | 32000 |
| Number of grid points | 256 | | | | | | | | 768 | 800 | 1000 | 1440 | 1440 | 2000 | 4000 |

For $\gamma \in [0.001, 0.2]$, **Fig. 8** shows the result of 100,000 standard/unbiased Monte Carlo realizations for $\gamma \leq 0.15$ and for 40,000 realizations for $\gamma > 0.15$. The curve can be approximately described as

$$R1(\gamma) = 0.5494 \log(\gamma) - 0.8937 \tag{28}$$

with $r^2 = 0.9434$. Note that for large scaled wave power, the probability increases with $\gamma$ while the opposite holds for small scaled wave power.
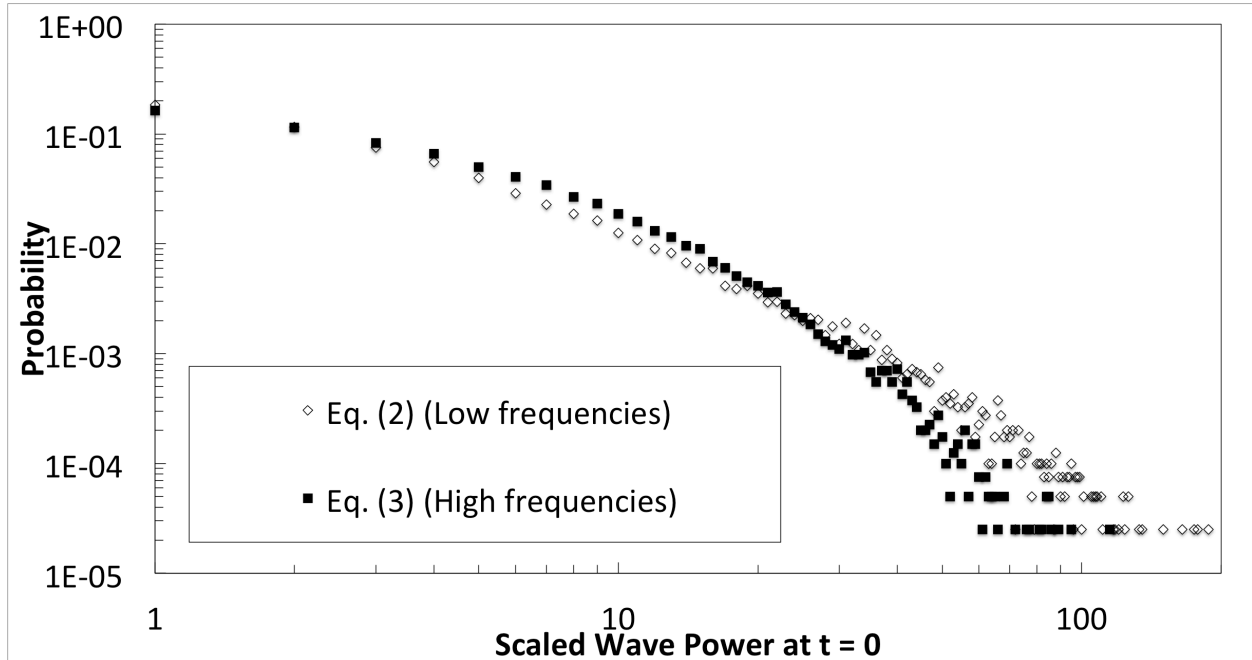


**Figure. 9**: The pdf of the scaled wave power for low and high frequency excitations.

**Fig. 9** compares the pdf generated from the fields resulting from propagating 40,000 realizations of the low and high frequency initial fields in (7) and (8) a scaled propagation distance of 8 units with the RKHD for $\gamma = 0.125$, 8000 propagation steps and 1440 grid points (similar results apply for $\gamma$ in the range $[0.01, 0.15]$). This result demonstrates the decreased strong self-focusing and hence rogue wave probability for initial fields composed of numerous high frequency waves.

While the pdf of the scaled maximum wave power is more affected by nonlinearity than the pdf of the scaled wave power result above, as evident from **Fig. 10**, which is obtained from the lower frequency excitation of (7) and 40,000 realizations, this is accompanied by a far larger variation among the probabilities in the rogue wave region. As well, larger nonlinearities are seen to generate higher power rogue waves.
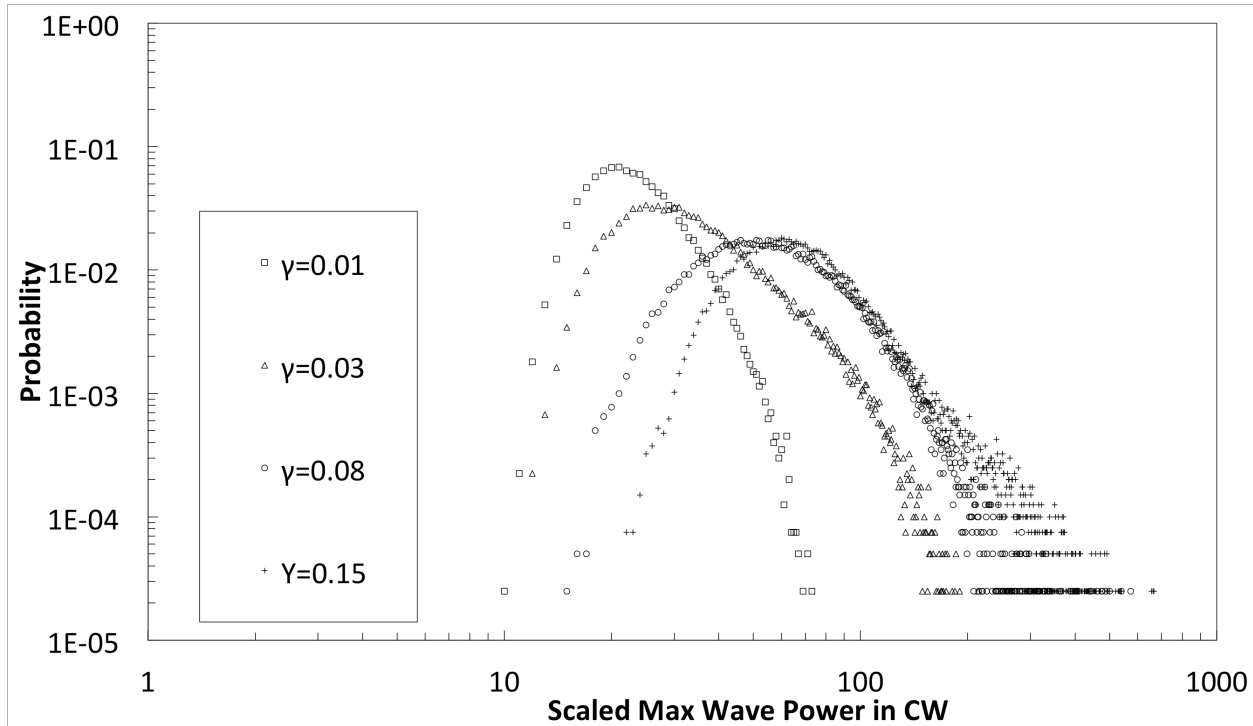
**Figure. 10**: The pdf of the scaled maximum wave power according to the maximum wave power metric as generated with the RKHD in **Table. 4**.

**Table. 4**

| $\gamma$ | 0.01 | 0.03 | 0.08 | 0.15 |
|---|---|---|---|---|
| Number of propagation steps | 250 | | 2640 | 8000 |
| Number of grid points | 256 | | 800 | 1440 |

## 4.2 Monte Carlo analysis of oceanic wave

The results of 40,000 Monte Carlo realizations of oceanic model are summarized in **Table. 5**, which show the percentage of rogue waves for different values of $\chi$ and $\gamma$. In these calculations, the heights of $\approx 2.8 \times 10^6$ waves in the propagated field were employed to calculate the percentage of rogue waves for each pair of $\gamma$ and $\chi$.

**Table. 5**: Percentage of rogue waves for each pair of values ($\gamma$, $\chi$).

| Percentage of rogue wave ($10^{-2}$%) $\gamma$ | $\chi$ | 3 | 4 | 5 | 6 | 7 | 8 |
|---|---|---|---|---|---|---|---|
| 0.03 | | 0.42355 | 0.61880 | 0.90383 | 1.29244 | 1.67242 | 1.98333 |
| 0.05 | | 0.15055 | 0.22206 | 0.30267 | 0.39242 | 0.47631 | 0.45888 |
| 0.08 | | 1.12078 | 1.48125 | 1.89231 | 2.19624 | 2.50104 | 2.69048 |

24

| 0.10 | | 0.86236 | 1.12474 | 1.30619 | 1.58069 | 1.77161 | 2.04224 |
|------|---|---------|---------|---------|---------|---------|---------|
| 0.125 | | 1.40155 | 1.73159 | 1.95333 | 2.29704 | 2.39546 | 2.64244 |
| 0.15 | | 1.30462 | 1.67669 | 1.82511 | 2.02752 | 2.13966 | 2.28798 |
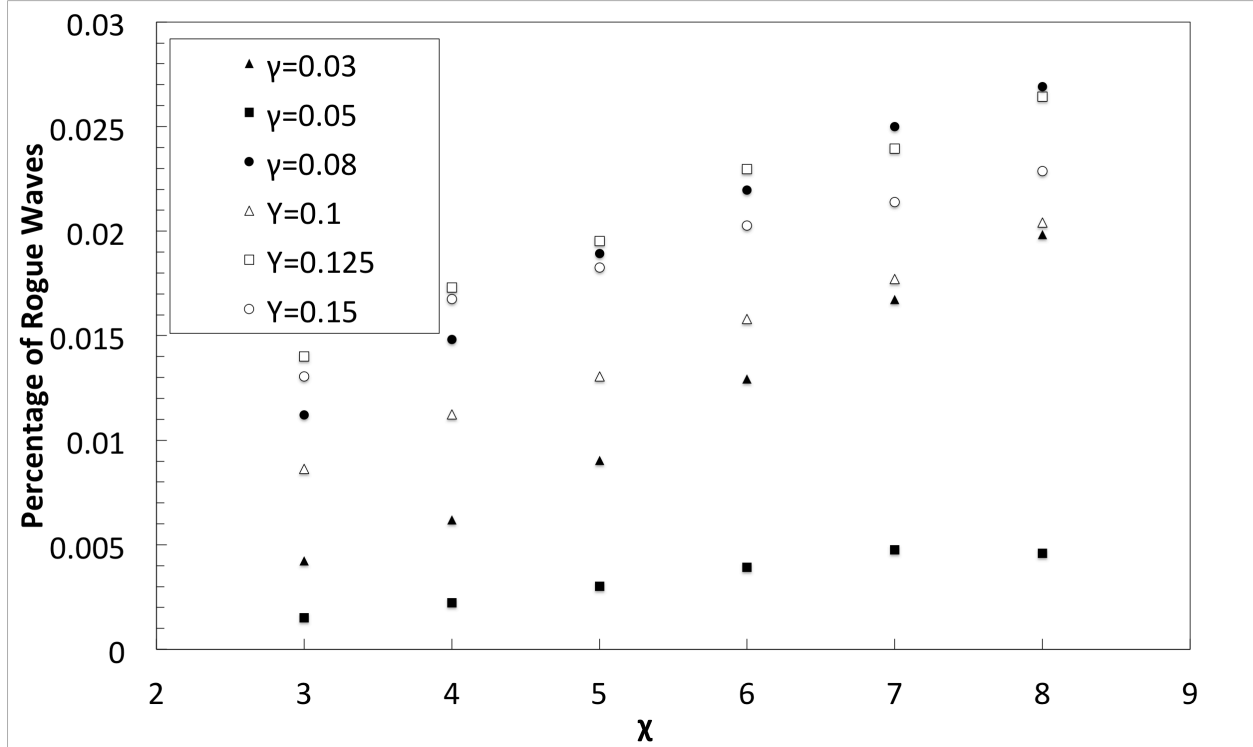


**Figure. 11**: The percentage of rogue waves for different $\chi$ and $\gamma$ in (9) for a scaled propagation distance equal to 8, and a computational window of 51.2 where the RKHD is employed with 8000 propagation steps and 1440 grid points.

**Fig. 11**, which displays the percentage of rogue waves for each pair of values $\chi$ and $\gamma$, demonstrates that the percentage of rogue wave increases with $\chi$ (except for the isolated cases $\gamma = 0.05, \chi = 7,8$, which will be analyzed in detail in section 4.6). [10] To understand this behavior, note that since the scaled energy in the computational window is constant, as the amplitudes of wave components whose frequencies are near or below $f_{peak}$, (the low frequency area in our model) increase with $\chi$, the power in the remaining wave components is simultaneously reduced. Therefore, in agreement with **Fig. 9**, where initial fields composed of numerous low frequency waves generate a larger fraction of rogue waves, the probability of large amplitude waves is enhanced, yielding the result of **Fig. 11**.

## 4.3 Optical Multicanonical Results

The multicanonical procedure is next employed to extend the results of section 4.1 to higher rogue wave powers. Evidently, although the nonlinearity enhances the rogue wave probability to a greater extent at large powers, the general trends are similar in high and low probability regions. However, as is also apparent from the Multicanonical Monte Carlo calculations with the parameters in **Table. 6** as displayed in **Fig. 12**, the rogue wave

probability becomes increasingly independent of $\gamma$ as $\gamma \rightarrow 0.1$. Additionally, the parameters in **Table. 6** insure that the pdfs generated by the standard/unbiased Monte Carlo and multicanonical procedures coincide for probabilities larger than $10^{-4} - 10^{-5}$.
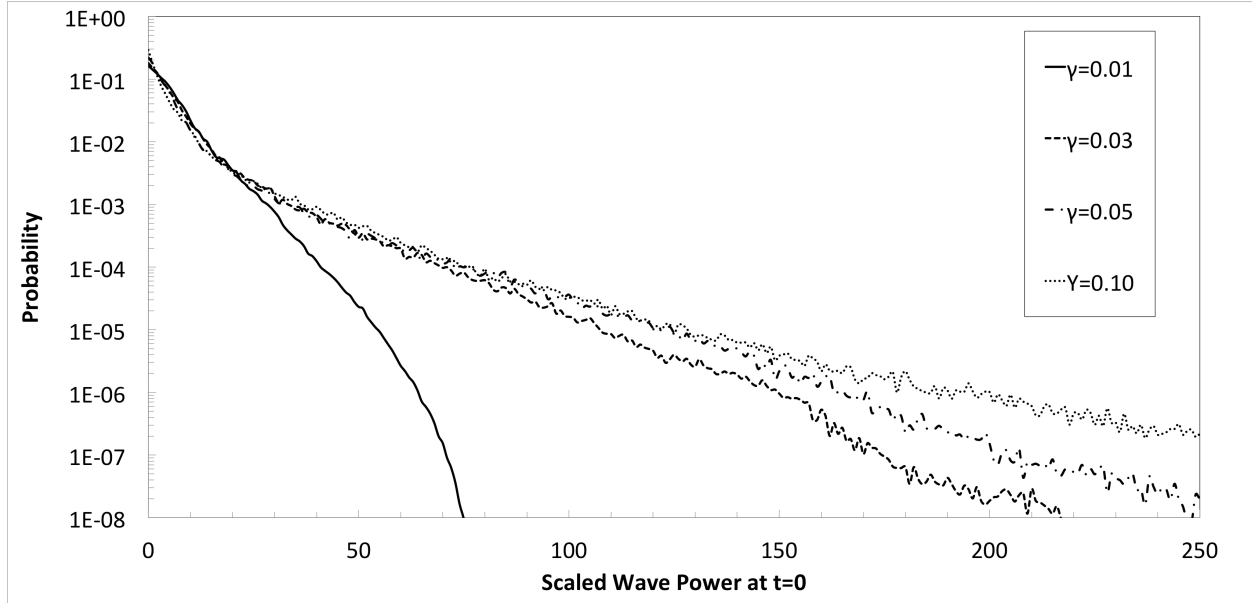


**Figure. 12:** The pdf of the scaled wave power for unit bins where (7) is applied in the first realization.

**Table. 6**

| $\gamma$ | Number of iterations | Realization number of nth iteration | Initial $\varepsilon$, $\varepsilon_0$ | $\varepsilon$ of nth iteration, $\varepsilon_n$ | | Initial bin value | Number of propagation steps | Number of grid points |
|---|---|---|---|---|---|---|---|---|
| | | | | Acceptance rate in (n-1)th iteration < 0.3 | Acceptance rate in (n-1)th iteration > 0.3 | | | |
| 0.01 | 4 | $10,000 \cdot 1.36^{n-1}$ | 0.2 | $1.05^{-1} \cdot \varepsilon_{n-1}$ | $1.05 \cdot \varepsilon_{n-1}$ | 1 | 250 | 256 |
| 0.03 | | | | | | | | |
| 0.05 | | | | | | | 1000 | 500 |
| 0.10 | | | 0.1 | | | | 4000 | 1000 |

## 4.4 Oceanic Multicanonical Results

In examining the pdf of ocean waves, the wave height at a specified fixed point in the computational window can conveniently be quantified as the relative wave height defined in Chapter 3. **Fig. 13** presents the multicanonical results for the pdf of the relative wave heights at $t$=0 for six values of the nonlinearity parameter $\gamma$, again confirming the marked dependence of the rogue wave probability on nonlinearity. As indicated in Chapter 3, the

parameters of **Table. 7** additionally yield standard/unbiased Monte Carlo and Multicanonical Monte Carlo pdfs that effectively match in the region for which the calculated probability exceeds $10^{-4} - 10^{-5}$. The multicanonical method determines the distributions for wave heights considerably greater than the square root of the average of the minimum squared rogue wave height. The results of **Fig. 13** were calculated with a bin width equal to 0.1, the updating schedule for $\varepsilon$ and number of realizations of **Table. 7** with 4 iterations and $\chi = 8$. In **Fig. 13** several values of $\gamma$ between 0.03 and 0.15 are considered. The discontinuity at zero relative wave height results from the definition of this quantity and has been verified through a standard Monte-Carlo calculation.

The height of a random sea wave can also be described by the scaled square of the maximum wave height in the computational window. The pdf of this quantity, obtained with four 25,000-sample iterations with $\gamma = 0.15$, c.f. **Table. 7**, is shown in **Fig. 14**. The position, 195, of the labeled vertical axis coincides with the average of the square of the minimum scaled rogue wave height. It should be remarked here that the parameters for the pdf of the squared maximum wave height are inappropriate for generating the pdf of the relative wave height. In particular, since the relative wave height is determined by the local behavior of the wave, a large number of intermediate histogram bins near the tail may remain unsampled yielding a fictitious increase in the pdf. This additionally explains our choice of the alternate set of parameters in the majority of our Multicanonical Monte Carlo calculations.

**Table. 7**: Parameters of Multicanonical Monte Carlo in **Fig. 13** and **Fig.14**

| $\gamma$ | Number of iterations | Realization number of nth iteration | Initial $\varepsilon$, $\varepsilon_0$ | $\varepsilon$ of nth iteration, $\varepsilon_n$ | | Initial bin value | Number of propagation steps | Number of grid points |
|---|---|---|---|---|---|---|---|---|
| | | | | Acceptance rate in (n-1)th iteration < 0.3 | Acceptance rate in (n-1)th iteration > 0.3 | | | |
| 0.03, 0.05, 0.08, 0.10, 0.125 0.15 | 4 | $10,000 \cdot 1.36^{n-1}$ | 0.1 | $1.05^{-1} \cdot \varepsilon_{n-1}$ | $1.05 \cdot \varepsilon_{n-1}$ | 1 | 8000 | 1440 |
| 0.15 | | 25000 | | | | 0 | | |
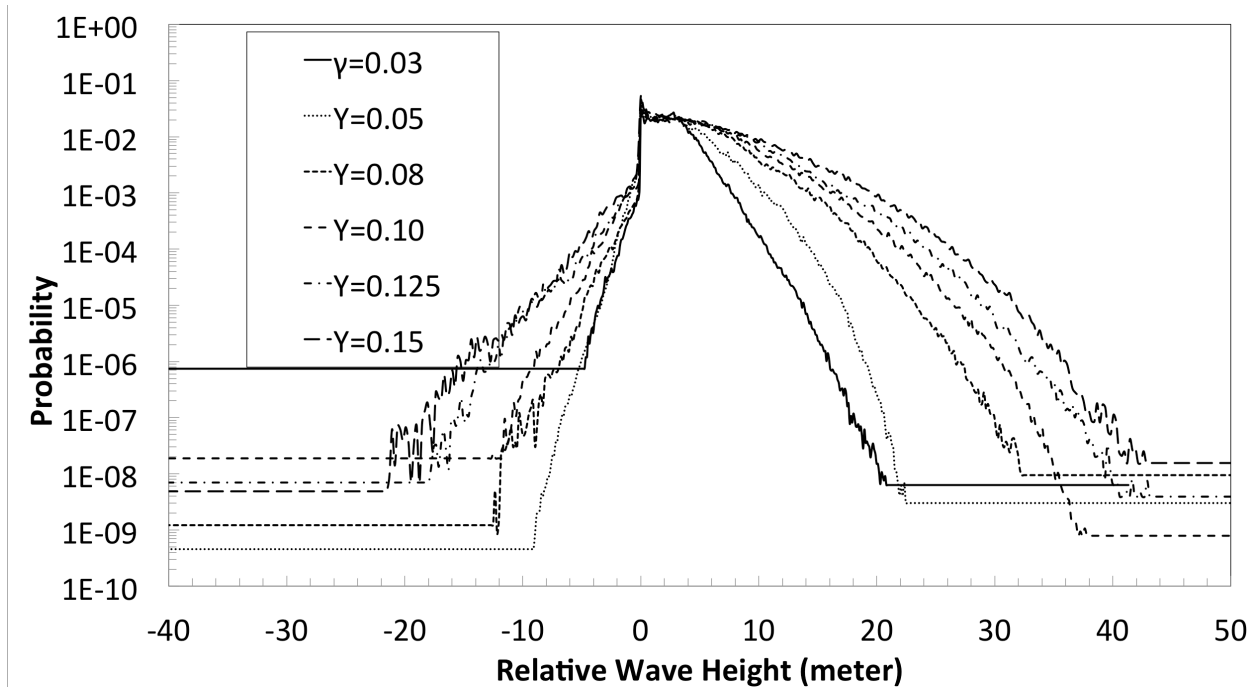
**Figure. 13**: The pdf of the relative wave height with bin width $0.1 \cdot \dfrac{v \Delta \omega \sqrt{2\gamma}}{k_0 \omega_0}$ , where (11) is applied in the first realization with $\chi = 8$ and the multicanonical procedure is employed with the parameters of **Table. 7**.
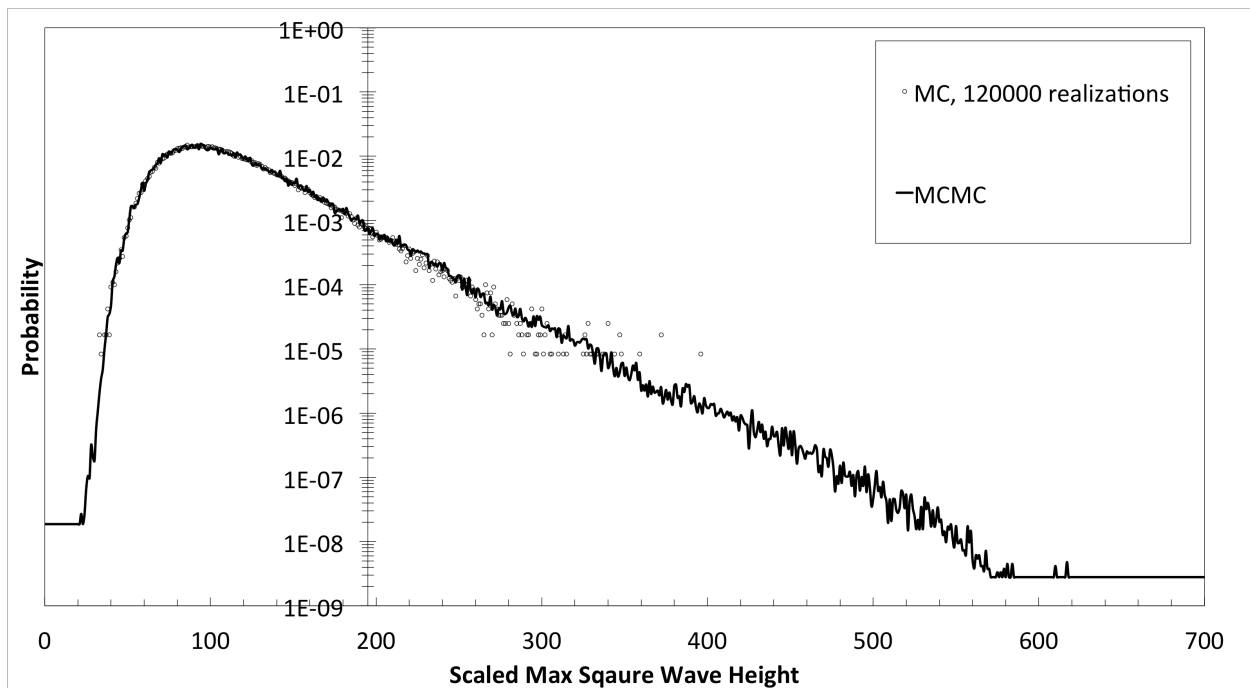


**Figure. 14**: The pdf of the relative wave height with unit bin width. (11) is applied in the first realization with $\chi = 8$ and $\gamma = 0.15$ and the Multicanonical Monte Carlo parameters of **Table. 7**. The vertical axis crosses the horizontal axis at 195, the average of the square of the minimum scaled rogue wave height.

## 4.5 Remark on the multicanonical results

Since the Multicanonical Monte Carlo results cannot be compared directly to theoretical results in sections 4.3 and 4.4, the method can only be verified by a comparison with the standard unbiased Monte Carlo technique as in **Fig. 13**. For $\gamma = 0.15$ these procedures are in good agreement. Indeed, for such problems in which analytic solutions are not available, the unbiased Monte Carlo results are generally treated as experimental data [9][11][28] [29]. In fact, as mentioned in [28], the theoretical determination of the pdf of wave heights has not been solved yet for nonlinear propagation as for example, [29] reports that theoretical results for the wave envelopes is "somewhat poor, particularly in the presence of relatively strong instability" and mentions with reference to **Figs 2** and **4** in [29] that the analytic solutions are particularly accurate in low probability regions. Since in order to increase the occurrence of rogue waves, the methods of this thesis are generally applied to highly nonlinear waves with a probability of occurrence lower than $10^{-4}$ our results cannot be reliably compared to analytic solutions. As well, in the linear case, the Rayleigh distribution requires that the wave height equal twice the wave crest. Otherwise the Rayleigh distribution generally overestimates the wave heights of large waves. [30]. Additionally since many linear propagation problems can be efficiently analyzed with the FFT, a comparison with the Monte Carlo results is not particularly meaningful in the linear regime.

## 4.6 Effects of nonlinearity

While recording the heights of $\approx 2.8 \times 10^{6}$ waves generated from 40,000 realizations in the absence of nonlinearity ($\gamma = 0$, $\chi = 8$) yielded only 7 rogue waves events, with nonlinearity present, thousands of rogue waves were generated as evident from **Table. 5**. This clearly confirms the significance of nonlinearity in rogue wave generation. An identical conclusion can be drawn from the discussion of wave power in sections 4.1 and 4.3. Additionally, in **Fig. 11**, the percentage of rogue waves is unexpectedly smaller at $\gamma = 0.05$ than at $\gamma = 0.03$. An analysis of the percentage of rogue waves for $\gamma = 0.05$ and different values of $\chi$ is presented in **Fig. 15**, which is computed with the RKHD for a scaled propagation distance of 8, 8000 propagation steps, 1440 grid points and a computational window of 51.2. This figure indicates that the probability of rogue waves does not vary monotonically with $\gamma$ but rather experiences a minimum for $\gamma \approx 0.05$. Because of the small value of the probability at this minimum, the results for the percentage of rogue waves at $\chi = 7, 8$ are susceptible to error, which presumably explains the anomalous results of **Fig. 11**.
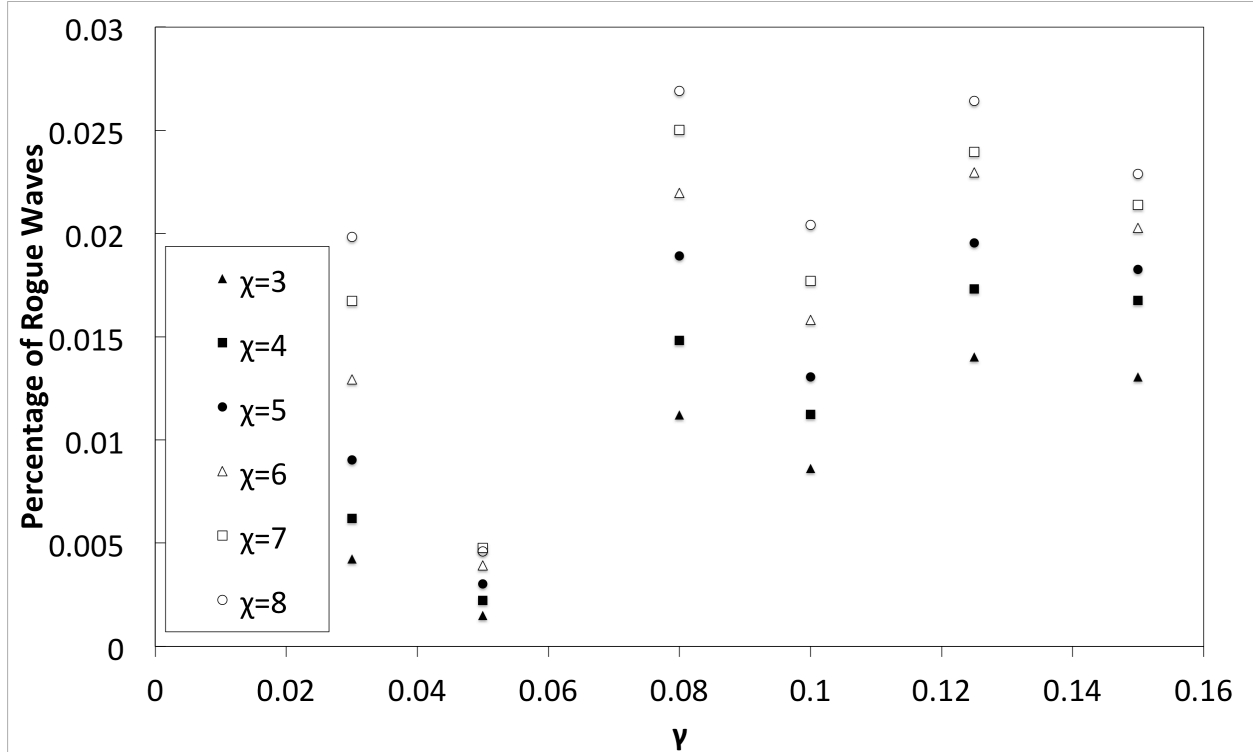
**Figure. 15**: The percentage of rogue waves for different $\chi$ and $\gamma$ in (9) for a scaled propagation distance equal to 8 and a computational window of 51.2 where the RKHD is employed with 8000 propagation steps and 1440 grid points.

Further studies show a similar trend for excitations with varying minimum rogue wave height and $\chi$ values as illustrated by the pdf of the scaled wave height, **Fig. 16**, for $\gamma = 0.03$ and $\gamma = 0.05$. This figure employs (11) to generate the first realization, and $10,000 \cdot 1.36^{n-1}$ samples for the $n$th iteration together with the acceptance rate of **Fig. 12**. The vertical axis is positioned at a scaled relative wave height of 13, which is the square root of the average of the minimum rogue wave height square for $\gamma = 0.03$. Further studies indicate that the average of the square of the scaled minimum rogue wave height attains a minimum ($\sim$170) at $\gamma = 0.03$ and a maximum ($\sim$205) at $\gamma = 0.05$. **Fig. 16** demonstrates that this unexpected behavior still exists even if the scaled minimum rogue wave heights are both set to an identical value, here 13. As the multicanonical procedure additionally extends the pdf of relative wave height to the rare probability region in **Fig. 16** this behavior cannot be attributed to undersampling.
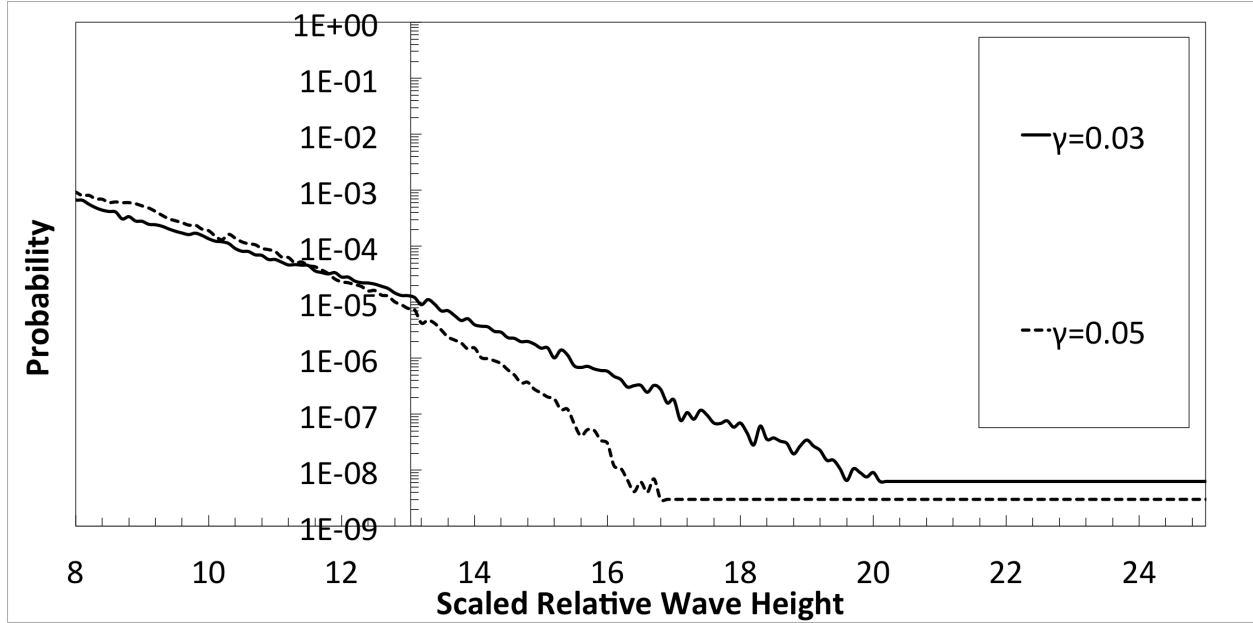
**Figure. 16**: The pdf of relative wave height for $\chi = 8, \gamma = 0.03, 0.05$ and a bin width of 0.1. The vertical axis crosses the horizontal axis at 13, the square root of the average of the square of the minimum scaled rogue wave height for $\gamma = 0.03$.

The origin of the anomalous features becomes apparent from the frequency spectrum displayed in **Fig. 17** and **Fig. 18** of the propagated field, $\mathrm{Re}\left[ A(z,t) \exp\left(2\pi f_{\mathrm{peak}} t\right)\right]$, obtained after scaled propagation distances of 8, 40, and 80 when (11) together with a set of 500 random phases is employed as the initial condition. In this figure the soliton period and total scaled energy equal $0.5\pi$ and 256, respectively while $\gamma = 0.03$, $\chi = 8$, $\Delta t = 0.025$ and $\Delta z$ is set slightly below the stability limit.
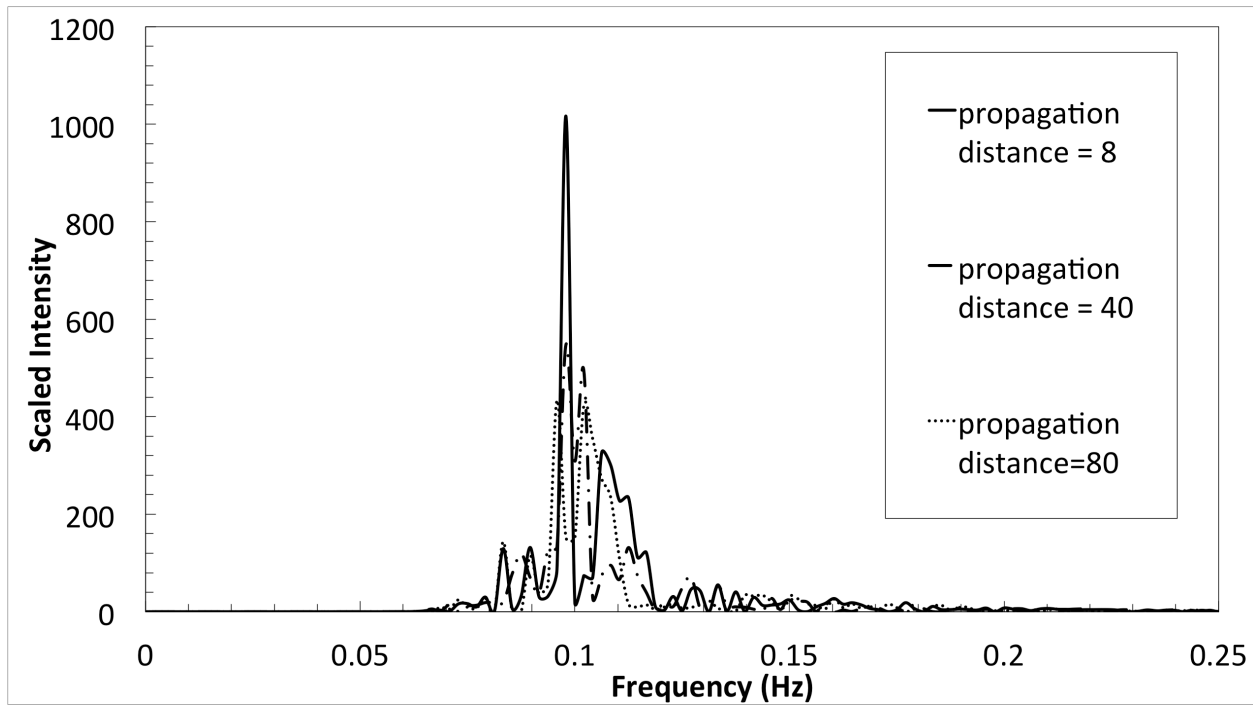
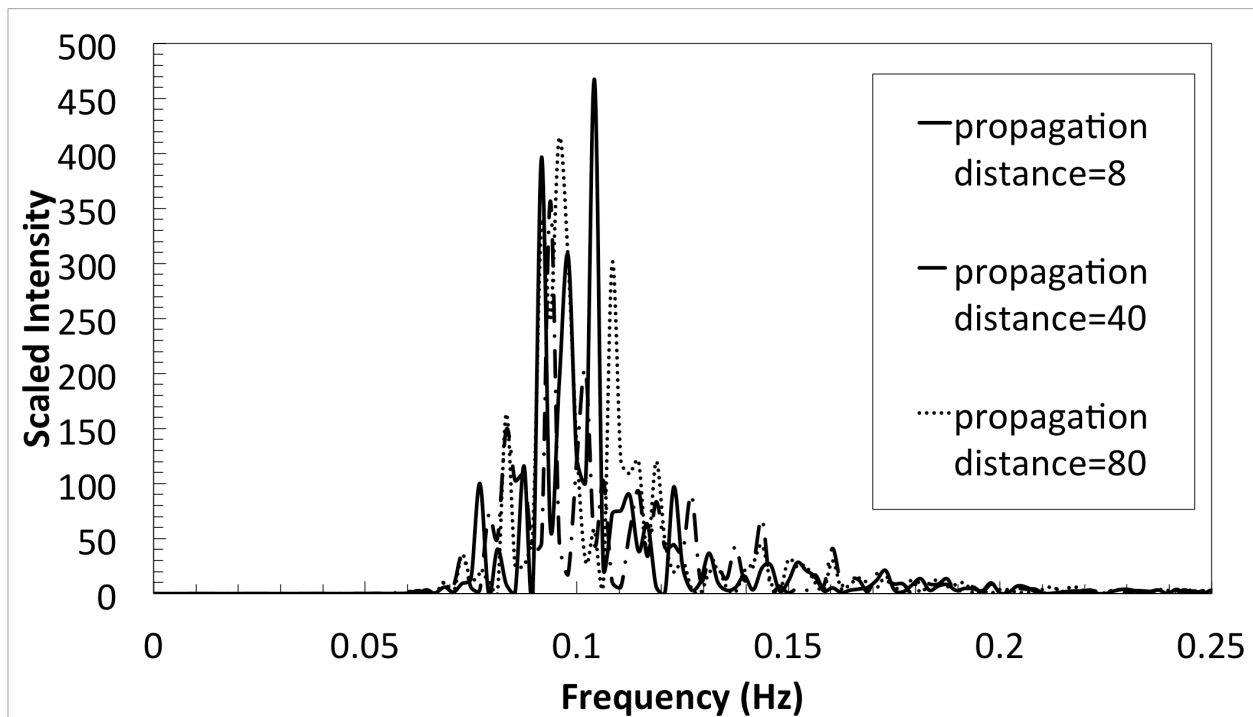**Figure. 17**: The propagated field spectrum for $\gamma = 0.03$.



**Figure. 18**: The propagated field spectrum for $\gamma = 0.05$.

As can be seen in **Fig. 17** at a propagation distance of 8 normalized units, for $\gamma = 0.03$ a maximum is present near 0.1Hz that is absent at longer propagation distances as well as in

32

the $\gamma = 0.5$ spectrum of **Fig. 18**. At the longer distances, the spectra broaden such that the average width is larger at higher $\gamma$. As well, the width is greater for $\gamma = 0.03$ than for $\gamma = 0.05$, yielding an increased rogue wave probability. Hence, the apparent anomalous result for the percentage of rogue waves at $\gamma = 0.03$ in **Fig. 17** can be associated with the small propagation length.

Furthermore, as evident for example in **Fig. 15**, the rogue wave pdf varies relatively slowly with the nonlinear coefficient for $\gamma > 0.08$. More generally, the pdf of the wave height often initially increases with $\gamma$ but then diminishes past a certain "crossing point". As a result, for waves with heights below the value associated with the crossing point, rogue waves are suppressed at larger $\gamma$. In [11] this effect is attributed to both a nonlinear broadening of the frequency spectrum, which yields larger probabilities for highly peaked excitations and to the low frequency flattened pulses resulting from the redistribution of energy over the computational window according to the Matthew effect: the less will be less and the more will be more.

# Chapter 5
# Drag Probabilities

In this chapter, we examine the predictions for the drag probabilities in the context of the model of Chapters 2 and 3, focusing on the drag probabilities associated with a perturbed obstacle. In section 5.1 we calculate the pdf of the drag in very rare probability areas and follow this in section 5.2 with a study of the drag probabilities of a noise-perturbed inlet and a moving obstacle. These results are then shown to be in good agreement with those of the standard unbiased Monte Carlo method.    While as in Chapter 4, these results cannot be obtained analytically, they are confirmed through a comparison to an "induction" method for the exact probability of the smallest drags in section 5.3 as well as to physical arguments in section 5.4, where the relationship between different surface configurations of the obstacle and the value of drags is discussed for the configurations associated with the highest and lowest pdfs.

## 5.1 Results of the multicanonical procedure
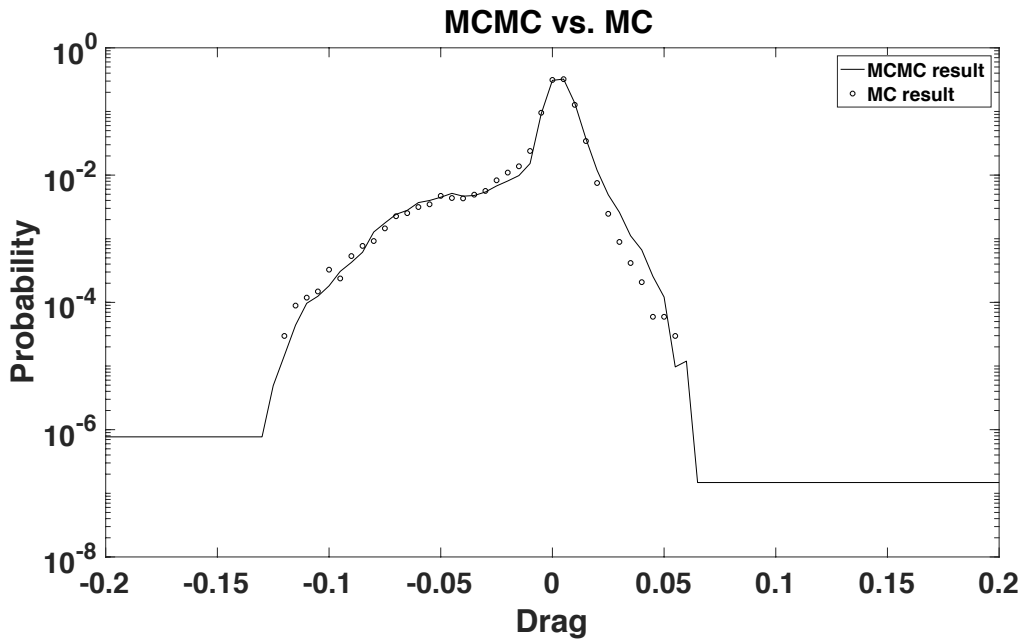


**Figure. 19** The pdfs of the drag for the case of a constant input flow velocity perturbed by a sum of 4 sinusoidal waves with randomly generated phases obtained with the standard Monte-Carlo method (diamonds) and three iterations with a total of 33677 realizations of the multicanonical procedure (solid line).
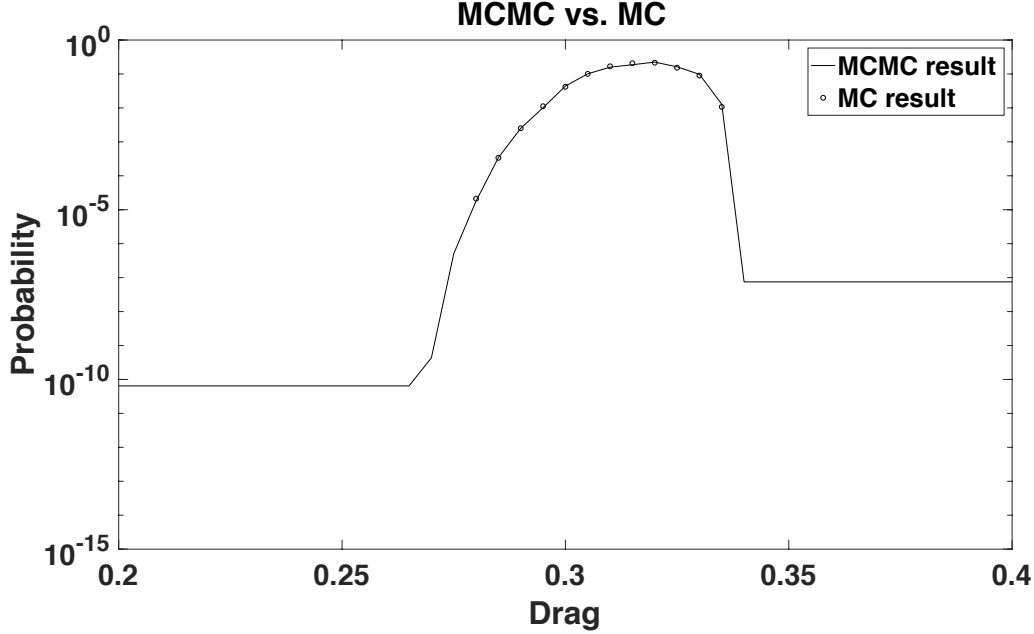
**Figure. 20** As in **Fig. 19** but for an obstacle with a randomly perturbed surface after four multicanonical Monte Carlo iterations with a total of 47219 realizations.
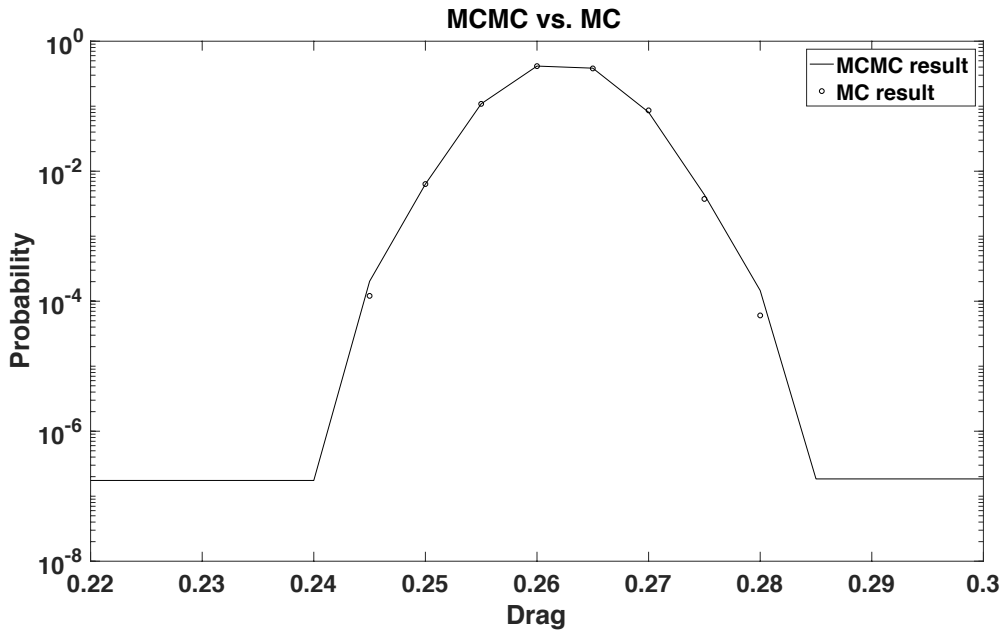
The pdfs obtained when the multicanonical method is applied to the drags associated with perturbing first the left boundary velocity and then the obstacle surface are displayed in **Figs. 19** and **20**, respectively for a histogram bin width of $5 \times 10^{-3}$. The results of **Fig. 19** were calculated with a total of 33677 realizations for both the standard (diamond markers) and three iterations of the multicanonical procedure (solid lines) while **Fig. 20** employed a total of 47219 realizations and four multicanonical iterations. While the multicanonical procedure effectively coincides with the Monte-Carlo results in the large probability region, the pdfs of **Fig. 20** are in significantly better agreement, extend to lower values and are generally smoother than those of **Fig. 19**. The loss of accuracy in **Fig. 19** is most likely associated with the discretization error arising from the highest frequency component of the input field (the fourth lowest plane wave). Further, since the momentum of the input field varies with the relative phases of the sinusoidal components of the input field, a small change in the phase coefficient significantly affects the drag and hence the pdf. This effect, which is more pronounced for small numbers of grid points, substantially contributes to the observed error in the multicanonical result at high drag values.

Perturbing the obstacle shape at a single grid point however only slightly changes the drag coefficient, insuring the accuracy of the multicanonical procedure. As well, in the high probability region of **Fig. 19**, the four components of the input field possess differing phases while the front end of the obstacle is not located at the maximum or minimum of the incoming wave. Hence a small phase change here does not substantially alter the drag.

## 5.2 Generality of the multicanonical procedure

To show the generality of the multicanonical procedure, we insert a $10 \times 10$ obstacle into a flow with an inlet velocity given by $U_{inlet} = (0.12 + noise \sim uniform[-0.01, 0.01])\hat{x}$. The model's

resolution is $50 \times 40$. The result is shown in the following figure.



**Figure. 21** The pdfs of the drag for a constant input flow velocity perturbed by noise as obtained with the standard Monte Carlo method (diamonds) and three iterations with a total of 16551 realizations of the multicanonical procedure (solid line).

This result demonstrates the efficiency of the multicanonical procedure for noisy inputs.. The result is consistent with earlier studies of Multicanonical Monte Carlo to various systems affected by noise. [31]

We also examined the case of a moving obstacle. For example, we considered the case that the inlet and obstacle velocities are offset by $U_{inlet} = 0.14\hat{x}$ and $U_{Obstacle} = 0.05\hat{x}$. For a $66 \times 60$ point grid with the same surface perturbations as above the results, which are given in the figure below demonstrate the applicability of the multicanonical method to this case. In fact, the fundamental property that ensures the applicability of the multicanonical procedure is the requirement that small changes in the initial/boundary conditions yield small changes of the final result that are sufficiently often accepted by the transition rule..

36
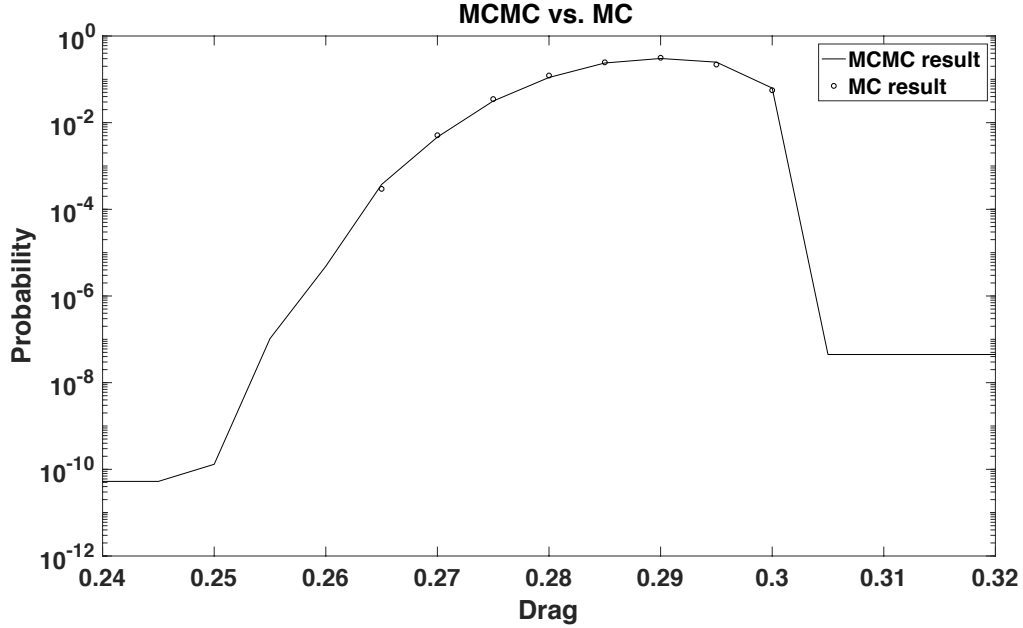
**Figure. 22** The pdfs of the drag for a constant input flow velocity and a moving obstacle with a randomly perturbed surface as computed with the standard Monte Carlo method (diamonds) and three iterations with a total of 47219 realizations of the multicanonical procedure (solid line).

## 5.3 Verification

The multicanonical results for the perturbed obstacle can be interpreted in the context of the drag, $D_0 = 0.263$, of the unperturbed obstacle with a length of 10 points in the transverse, *y*-direction and the corresponding drag, $D_1 = 0.332$, for the 12 transverse point rectangular obstacle obtained once all fluid points above and below the obstacle are converted to solid points. While the lower bound of the drag does not fall below $D_0$, presumably since enlarging the surface by a small number of grid points does not lead to a sufficiently streamlined profile, the corrugated, large area surface that emerges when a large number of nonadjacent fluid points are converted to solid points can generate a drag greater than $D_1$. Thus in **Fig. 22** the multicanonical pdf extends from a drag value of 0.266 which falls into the histogram bin $b_L \in (0.265, 0.270]$, and occurs with a probability of approximately $4.33 \times 10^{-10}$ to a value of 0.333 in $b_U = (0.330, 0.335]$ with a probability $\approx 1.28 \times 10^{-2}$.

To confirm the physical picture presented in the preceding paragraph, **Figs. 23** and **24** display the lowest and highest drag configurations generated by the multicanonical method. The first of these figures differs only at a single edge point from the minimum drag unperturbed state and is associated with a drag value that falls into the histogram bin (0.260, 0.265]. This suggests that for the small drag values closest to the origin of **Fig. 22**, the drag is strongly dependent on the surface geometry, which in turn enables the direct verification of the multicanonical pdf of the bin $b_L$. That is, when the number of fluid points, $n$, along the surface that have been converted to material points is small, an additional material point significantly increases the drag. Hence, all configurations with

37

$n+1$ surface points and drags in $b_L$, can be found by adding an additional surface point to the known configurations with $n$ surface points with drags in this bin. Starting from $n=1$, the 464 configurations enumerated in **Table. 8** with $n \leq 6$ were found to possess drag values in $b_L$, while for $n > 6$ all computed drags were larger than 0.270. That is, a total of 464 configurations possess drags in $b_L$ in the model compared to the $2^{40}$ configurations that are associated with the 40 grid points above and below the obstacle surface. Since the probability of a given configuration therefore equals $2^{-40}$, the probability of obtaining a drag in $b_L$ exceeds that of the single lowest drag state, $2^{-40} \approx 9.09 \times 10^{-13}$, by a factor of 464. The value, $4.22 \times 10^{-10}$, nearly coincides with the multicanonical prediction, $4.33 \times 10^{-10}$, verifying the accuracy of the multicanonical algorithm in the low probability region. Note that the rapid decrease in the number of configurations in $b_L$ as the number of additional surface points increases again indicates the large influence of surface geometry on the drag coefficient for small drag values.

**Table. 8**

| Total Number of Additional Surface Points, n | Number of Configurations with Drags in $b_L$ | Number of Possible Configurations | Conditional Probability of Drags in $b_L$ |
|---|---|---|---|
| 1 | 32 | $\begin{pmatrix} 40 \\ n \end{pmatrix}$ | $8 \times 10^{-1}$ |
| 2 | 242 | | $3.10 \times 10^{-1}$ |
| 3 | 50 | | $5.06 \times 10^{-3}$ |
| 4 | 108 | | $1.18 \times 10^{-3}$ |
| 5 | 28 | | $4.03 \times 10^{-5}$ |
| 6 | 4 | | $1.04 \times 10^{-6}$ |
| 7 | 0 | | 0 |
| >7 | 0 | | 0 |

### 5.4 Configurations and Drags

The multicanonical result for the maximum drag configuration is displayed in **Fig. 24** and as predicted displays a high level of corrugation, which enhances the frictional force relative to that of a simple enlarged rectangle. Note further that the magnitude of the slope of the pdf for small drags is far larger than that on the large drag side of the maxima, consistent with the considerably greater magnitude at low Reynolds number of the pressure-induced drag compared to the frictional drag. [32] The number of realizations is additionally limited for low drag values, as only a single state exists with the minimum drag while numerous highly corrugated states contribute with nearly similar drag values at the upper end of the pdf curve as a result of the relatively small frictional force.

As expected, the drag is reduced for streamlined objects that are enlarged near the front and back faces compared to the central region. Thus, the two configurations with large drags in **Figs. 24** and **25** are enlarged near the front and back while differing in geometry

near the middle of the obstacle. However, for configurations with narrow front and back regions and therefore small drag, such as in **Fig. 5**, the geometry near the center of the top and bottom facets can considerably affect the drag, as evident through a comparison with **Fig. 24** which possesses a much smaller drag coefficient despite its nearly identical geometry near the middle of the obstacle. Here the large number of dissimilar states that contribute to the same histogram bin for large drags precludes a direct verification of the multicanonical probability in contrast to the small drag case. The above results also clearly indicate that for an identical sample size and therefore calculation time the multicanonical procedure both reproduces the standard/unbiased Monte Carlo results in the high probability region and extends the dynamic range of the method by several orders of magnitude.
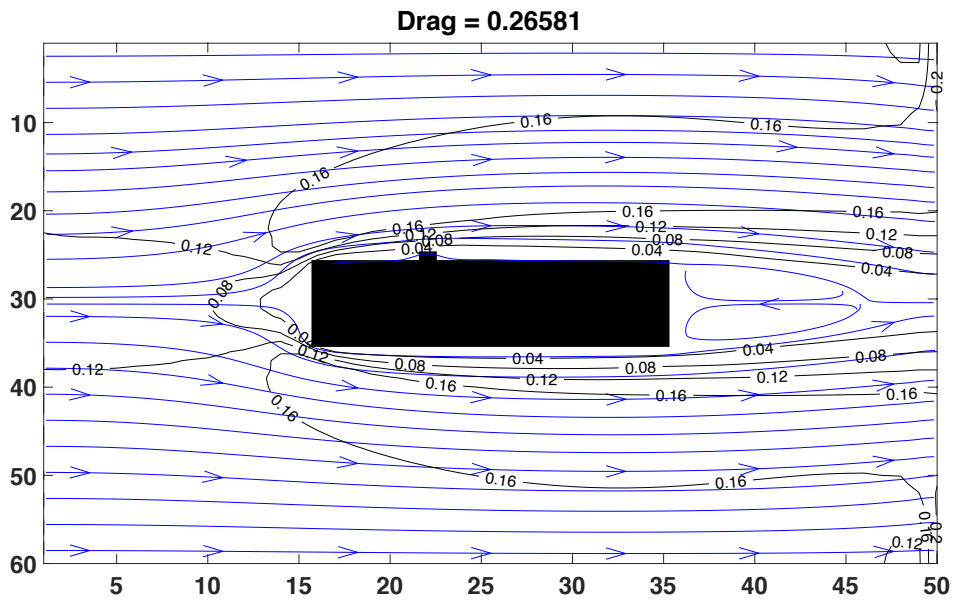


**Figure. 23** The steady state velocity profile generated by the minimum drag realization obtained for the perturbed rectangular obstacle with the multicanonical Monte Carlo procedure.
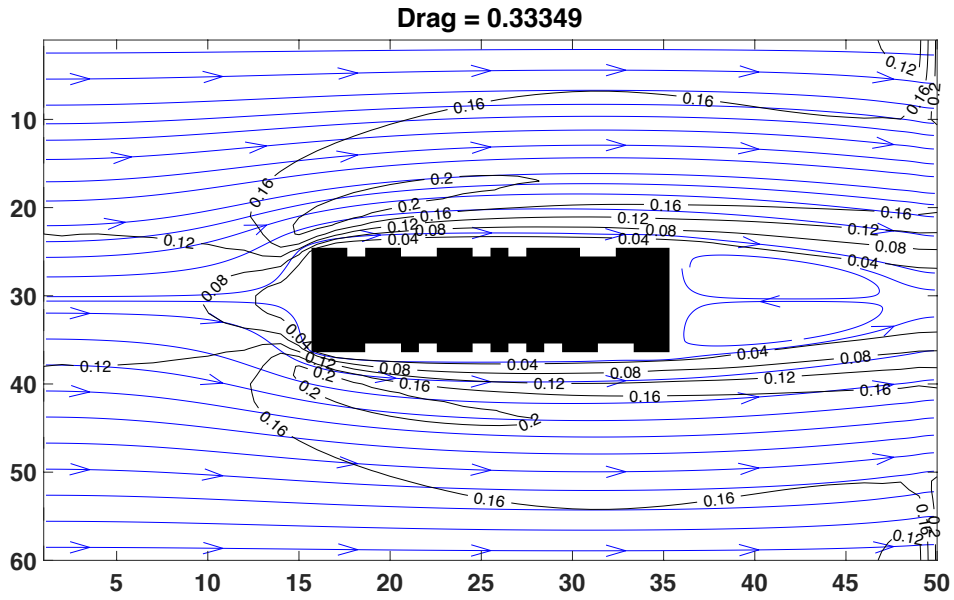
**Drag = 0.33349**



**Figure. 24** As in **Fig. 23** but for the maximum drag realization.
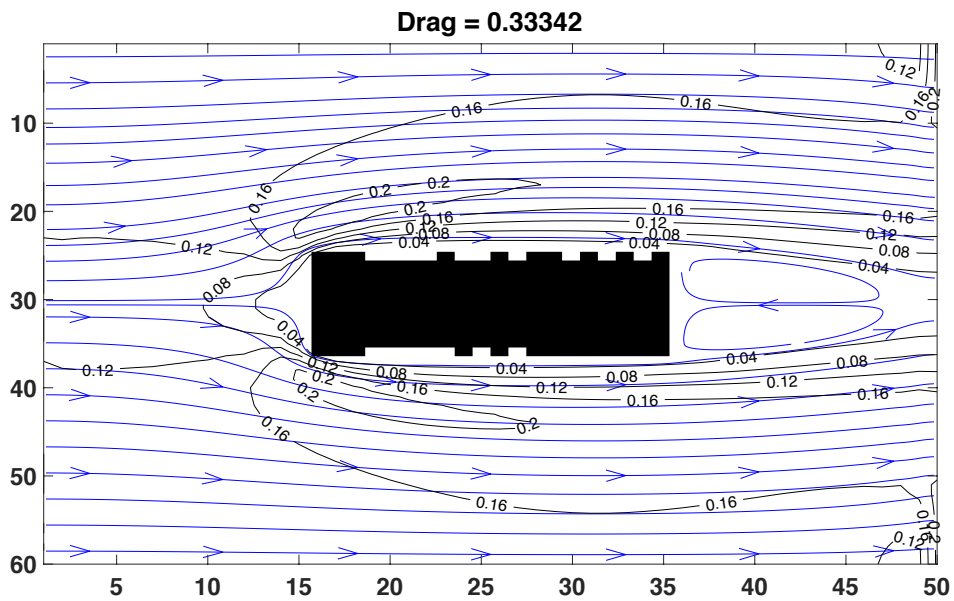
**Drag = 0.33342**



**Figure. 25** As in **Fig. 23** but for a realization with a drag close to the maximum value.

# Chapter 6
# Conclusions

**6.1 RKHD, Multicanonical Monte Carlo, and Nonlinearit**y
In this thesis we have advanced several methods for improving the analysis of rogue wave probabilities. The propagation algorithm for the Nonlinear Schrödinger Equation was first improved by introducing the RKHD.  Next, the multicanonical procedure enables the pdfs of wave power and wave heights to be evaluated highly efficiently. Accordingly, the pdfs of the wave heights can be evaluated even in probability regions that are far lower than those commonly associated with the appearance of rogue waves.  Additionally, we advanced a finite difference based Runge-Kutta procedure that was found to be more rapid than standard FFT based Runge-Kutta interaction procedures, especially for large propagation distances and high soliton orders.  This should enable the evaluation of fields after very long-range propagation distances or times.

Here we found that the generation probability for rogue waves is greater in the presence of low frequency initial fields than if only high frequency components are present. This conclusion is clearly consistent with both ideal model and the oceanic model. As well, we observed a logarithmic dependence of the slope of the pdf for large heights on the nonlinearity coefficient, which shows that the contribution of nonlinearity to the generation of high power waves decreases with increasing nonlinearity coefficient. This phenomenon is predicted by both of the ideal model and the oceanic model.

Last but not the least, we confirmed the applicability of Multicanonical Monte Carlo in oceanic contexts. As mentioned    at the end of [10], for more realistic models, the procedure that we employed to generate **Figs. 13** and **14** could be applied to determine the probabilities that a wave with a much higher amplitude than the commonly accepted cutoff amplitude of rogue waves appears at a certain distance from the observer. This is a significant quantity for oceanic platform designs.

**6.2 Suitability of the multicanonical procedure for drag probabilities**
While the calculations of the multicanonical procedure principally demonstrate the efficiency of the multicanonical algorithm in combination with the lattice Boltzmann procedure, that the probabilities of statistically unlikely but physically significant configurations can be rapidly determined in this fashion suggests numerous practical applications.  For example, the deformations of a wing resulting from local environmental changes that yield an unacceptably large drag would be difficult to characterize experimentally because of the large number of possible configurations. However, a multicanonical simulation could isolate such cases within a relatively limited amount of computation time if the underlying requirements of the procedure are satisfied.

**6.3 Comments on Multicanonical Monte Carlo**

Although sampling the high probability areas does not lead to a substantial increase in the relative accuracy, it does increase the overall quality of the result. However, in

Multicanonical Monte Carlo, when a new state is rejected, the previous state will become the new state, so that the transition does not contribute to the quality of the pdf. Since the optimal acceptance rate is typically approximated by a number close to 25%, roughly ¾ of the transitions are only required to drive the Markov chain toward low probability regions but do not simultaneously contribute to the accuracy of the pdf. This issue can be addressed by constructing a transition matrix as demonstrated in [22] but at the cost of program complexity and memory utilization.

According to [33], the accuracy of all Markov Chain Monte Carlo calculations should be established by joint distribution tests. Since the sampling method employed by the MMC is identical to that of the Markov Chain Monte Carlo a joint distribution test could similarly be of value in every application of Multicanonical Monte Carlo.

Smoothing the histogram by including contributions from a few adjacent bins can improve the result substantially if the second derivatives of the exact pdf are large as demonstrated by Eq.(4) of [13]. In the original implementation of this idea by Berg, however, while pdfs with large second order derivatives are improved, the procedure was limited to two adjacent bins and therefore does not demonstrate the full applicability of the procedure. As well, such procedures lead to flattened tails but do not improve the overall sampling efficiency and hence the efficiency of the sampling method cannot be reliably estimated. Consequently such procedures were not considered in this thesis.

Our Multicanonical Monte Carlo calculations are affected by a fundamental difficulty. While in problems with known pdfs such as analytic pdfs the Multicanonical Monte Carlo is highly efficient, if the pdfs are unknown, the Multicanonical Monte Carlo procedure requires the techniques in Chapter 2 to generate reliable results that however often exhibit fluctuations in their tail regions. However, problems for which the pdf is unknown correspond to the most important applications the Multicanonical Monte Carlo procedure. Accordingly, the issue of how to determine the accuracy of Multicanonical Monte Carlo results constitutes a fundamental issue. Firstly, when the pdfs are unknown, the accuracy of the Multicanonical Monte Carlo calculation is difficult to determine. Additionally the computation time may be insufficient to enable the sampling of low probability regions by the standard/unbiased Monte Carlo that can serve as a reference calculation. Hence, most applications of Multicanonical Monte Carlo cannot be tested directly. However, alternative methods of verification can be constructed if the pdf can be derived in regions of very low probability.

It is further possible to improve the computational efficiency in some cases by restricting the sampling to regions of physical interest. [34] This is done by unconditionally rejecting states in high probability regions. This leads to a conditional pdf which although was the quantity of interest in e.g. [34] can also be combined with sampling results in other regions to generate the full pdf. [35] Along these lines, I attempted to generate conditional pdfs by rejecting states from areas in which the pdfs obtained in two successive iterations were in good agreement. These conditional probabilities were then combined to generate the full pdf. While this procedure more efficiently directs the Markov chain into regions of low

probability and low accuracy, I found that the small errors in the conditional probabilities degraded the overall result for the pdf.

## 6.4 Proposals for future work

The Lattice Boltzmann model of Chapter 2 and Chapter 3 can only be applied to low Reynolds number flows.  Hence the drags computed in Chapter 5 pertain to Reynolds number of approximately 40 Reynolds corresponding to laminar flows. To adapt our method to for example aerodynamically interesting problems, the Reynolds number should be increased to at least $10^3$ in order to generate transient or turbulent flows. Unfortunately, two challenges appear when we extend the multicanonical procedure to the prediction of drag probability associated high Reynolds number flows for more complex systems such as realistic airfoils. In particular, displacing a small surface region significantly alters the computed drag and hence degrades the accuracy of the multicanonical method. However, if appropriate methods can be found for implementing the boundary condition and the Lattice Boltzmann formalism and that also ensure Markov Chain transitions yield small changes in the output variables of interest, the methods of this thesis could be extended as well to high Reynolds number flows.

# References

[1] N. Metropolis, A. W. Rosenbluth, M. N. Rosenbluth, A. H. Teller, *Equation of State Calculations by Fast Computing machines*, *The Journal of Chemical Physics*, Volume 21, Number 6. Pages 1087-1092, 1953.

[2] B. A. Berg, T. Neuhaus, *Multicanonical Ensemble: A New Approach to Simulate First-Order Phase Transitions*, *Physics Review Letter*, Volume 68, Number 1. Page 9, 1992.

[3] B. A. Berg, *Algorithmic Aspects of Multicanonical Simulations*, *Nuclear Physics B – Proceedings Supplements*, Volume 63, Number 1-3, Pages 982-984, proceedings of the XVth International symposium on Lattice Field Theory, 1998

[4] P. Wijesinghe, U. Gunawardana, R. Liyanapathirana, *Multicanonical Estimation of Outage Probabilities in MIMO Channels. GLOBECOM - IEEE Global Telecommunications Conference.* 1-5. 10.1109/GLOCOM.2010.5683948, 2010

[5] D. Yevick, "Multicanonical Communication System Modeling-application to PMD Statistics," *IEEE Photonics Technology Letters*, Volume 14, Number 11, Pages 1512-1514, 2002.

[6] R. Holzlohner, C. R. Menyuk, "Use of Multicanonical Monte Carlo Simulations to Obtain Accurate Bit Error Rates in Optical Communication System," *Optics letters*, Volume 28, Number 20, Pages 1894-1896, 2003.

[7] M. Tong, D. Yevick, *Multicanonical Analysis of Rogue Wave Probabilities*, *Wave Motion*, Volume 66, Pages 56-67, 2016

[8] M. Tong, D. Yevick, *Multicanonical Monte Carlo evaluation of drag probability distribution functions*, *Physics of Fluids*, Volume 30, Number 3, Page 033605, 2018

[9] M. Taki, A. Mussot, A. Kudlinski, E. Louvergneaux, M. Kolobov, M. Douay, *Third-order dispersion for generating optical rogue solitons*, *Physics Letter A*, Volume 374, Pages 691–695, 2010

[10] M. Onorato, A. Osborne, M. Serio, S. Bertone, *Freak wave in random oceanic sea states*, *Physics Review Letter*, Volume 86, Pages 5831–5834, 2001

[11] D. Solli, C. Ropers, P. Koonath, B. Jalali, *Optical rogue waves*, *Nature*, Volume 450, Pages 1054–1057, 2007

[12] J. Hult, *A Fourth-Order Runge–Kutta in the Interaction Picture Method for Simulating Supercontinuum Generation in Optical Fibers*, *Journal of Lightwave Technology*, Volume 25, Page 3770-3775, 2007

[13] D. Yevick, *The Accuracy of Multicanonical Systerm Models*, *IEEE Photon Technology Letter*, Volume15, Pages 224-226, 2003

[14] X. Ulrich, D. Peters, *Loads and Propulsive Efficiency of A Flexible Airfoil Performing Sinusoidal Deformations*, *Journal of Fluids and Structures*, Volume 45, Pages 15-27, 2014

[15] Z. Wu, Y. Cao, M. Ismail, *Numerical Simulation of Airfoil Aerodynamic Penalties and Mechanisms in Heavy Rain*, *International Journal of Aerospace Engineering* Volume 2013, Article ID 590924, 2013

[16] F. Liu, S. Jiang, G. Chen, Y. Li, *Numerical Investigation on Vortex-Structure Interaction Generating Aerodynamic Noises for Rod-Airfoil Models,* *Mathematical Problems in Engineering*, Volume. 2017, Article ID 3704324, 2017

[17] W. Li, S. Krist, R. Campbell, *Transonic Airfoil Shape Optimization in Preliminary Design Environment*, *Journal of Aircraft*, Volume 43, Number 3, Pages 639-651, 2006

[18] B. Ernst, H. Schmitt, J. R. Seume, *Effect of Geometric Uncertainties on the Aerodynamic Characteristic of Offshore Wind Turbine Blades*, *Journal of Physics: Conference Series*, Volume 555, Conference 1. 2016

[19] R. Mei, D. Yu, W. Shyy, L. Luo, *Force Evaluation in the Lattice Boltzmann Method Involving Curved Geometry*, NASA/CR-2002-211662, 2002

[20] S. Izquierdo, P. Martínez-Lera, N. Fueyo, *Analysis of Open Boundary Effects in Unsteady Lattice Boltzmann Simulations*, *Computers & Mathematics with Applications*, Volume 58, Issue 5, Pages 914-921, 2009

[21] Q. Zou, X. He, *On Pressure and Velocity Boundary Conditions for the Lattice Boltzmann BGK Model*, *Physics of Fluids*, 9, Pages 1591-1598, 1997

[22] D. Yevick and M. Reimer, "Modified Transition Matrix Simulations of Communication Systems," *IEEE Communications Letters*, Volume 12, Number 10, Page 755-757, 2008

[23] N. Akhmediev, J.M. Soto-Crespo, A. Ankiewicz, *Extreme waves that appear from nowhere: on the nature of rogue waves*, *Physics Letter A*, 373, Page 2137-2145, 2009

[24] L. H. Holthuijsen. *Waves in Oceanic and Coastal Waters*, Cambridge University Press. 2007

[25] M. C. Sukop, D. T. Thorne, *Lattice Boltzmann Model: An Introduction for Geoscientists and Engineers*, Springer-Verlag Berlin Heidelberg, Pages. 55-66, 2006

[26] S. Succi, *The Lattice Boltzmann Equation: For Fluid Dynamics and Beyond*. Clarendon Press, 2001.

[27] T. Krüger, et al, *The Lattice Boltzmann Method, Graduate Texts in Physics*, Springer International Publishing Switzerland, Chapter 3, 4, 5, 7, 2017

[28] M.Onorato, S. Residori, U. Bortolozzo, A. Montina and F.T. Arecchi, *Rogue waves and their generating mechanisms in different physical contexts*, *Physics Reports*, Volume 528, Issue 2, Pages 47-90, 2013

[29] Z. Cherneva, M. A. Tayfun, C. G. Soares, *Statistics of nonlinear waves generated in an offshore wave basin*, Journal of Geophysical Research: Oceans banner, Volume 114, Issue C8, 2009

[30] M. A. Tayfun, F. Fedele, *Expected shape of extreme waves in storm seas*. In Proc. 26th OMAE Conf., 2007a, San Diego, Paper Number OMAE2007-29073, ASME, 2007

[31] B. Tromborg, M. Reimer and D. Yevick, *Multicanonical Evaluation of the Tails of the Probability Density Function of Semiconductor Optical Amplifier Output Power Fluctuations*, *IEEE Journal of Quantum Electronics*, Volume 46, Number 1, Pages 57-61, Jan. 2010.

[32] R. Mei, L. Luo, W. Shyy, *An Accurate Curved Boundary Treatment in the Lattice Boltzmann Method*, *Journal of Computational Physics*, Volume 155, Pages 307-330, 1999

[33] J. Geweke, *Getting It Right: Joint Distribution Tests of Posterior Simulators*, *Journal of the American Statistical Association*, Volume 99, Number 467, Pages. 799-804, 2004

[34] R. Holzlohner, A. Mahadevan, C. Menyuk, J. Morris, J. Zweck, *Evaluation of the Very Low Ber OF fec Codes Using Dual Adaptive Importance Sampling*, *IEEE Communications Letters*, Volume 9, Number 2, Pages 163-165, 2005

[35] M. Reimer, A. Awadalla, D. Yevick, and T. Lu, *Alignment Methods for Biased Multicanonical Sampling*, *Journal of the Optical Society of America A-Optics Image Science and Vision*, Volume 24, Number 8, Pages 2474-2479, 2007